

1 **Ensembling Differentiable Process-based and Data-driven Models with**  
2 **Diverse Meteorological Forcing Datasets to Advance Streamflow Simulation**

3 Peijun Li<sup>1</sup>, Yalan Song<sup>1</sup>, Ming Pan<sup>2</sup>, Kathryn Lawson<sup>1</sup>, Chaopeng Shen<sup>1</sup>

4 <sup>1</sup>Civil and Environmental Engineering, The Pennsylvania State University, University Park,  
5 PA, USA

6 <sup>2</sup>Center for Western Weather and Water Extremes, Scripps Institution of Oceanography,  
7 University of California San Diego, La Jolla, CA, USA

8 \*Correspondence to: Peijun Li, pql5336@psu.edu; Chaopeng Shen, cshen@engr.psu.edu

9  
10 **Abstract**  
11 Streamflow simulations produced by different hydrological models exhibit distinct  
12 characteristics and can provide valuable information when ensembled. However, few studies  
13 have focused on ensembling simulations from models with significant structural differences  
14 and evaluating them under both temporal and spatial tests. Here we systematically evaluated  
15 and utilized the simulations from two highly different models with great performances: a purely  
16 data-driven long short-term memory (LSTM) network and a physics-informed machine  
17 learning (“differentiable”) HBV (Hydrologiska Byråns Vattenbalansavdelning) model ( $\delta$ HBV).

18 To effectively display the features of the two models, multiple forcing datasets are employed.  
19 The results show that the simulations of LSTM and  $\delta$ HBV have distinct features and  
20 complement each other well, leading to better Nash-Sutcliffe model efficiency coefficients  
21 (NSE) and improved high-flow and low-flow metrics across all spatiotemporal tests, compared  
22 to within-class ensembles. Ensembling models trained on a single forcing outperformed a  
23 single model using fused forcings, challenging the paradigm of feeding all available data into  
24 a single data-driven model. Most notably,  $\delta$ HBV significantly enhanced spatial interpolation  
25 when incorporated into LSTM, and provided even more prominent benefits for spatial

26 extrapolation where the LSTM-only ensembles degraded significantly, attesting to the value of  
27 the structural constraints in  $\delta$ HBV. These advances set new benchmark records on the well-  
28 known CAMELS (Catchment Attributes and Meteorology for Large-sample Studies)  
29 hydrological dataset, reaching median NSE values of  $\sim 0.83$  for the temporal test (densely  
30 trained scenario),  $\sim 0.79$  for the ungauged basin test (PUB, Prediction in Ungauged Basins),  
31 and  $\sim 0.70$  for the ungauged region test (PUR, Prediction in Ungauged Regions). This study  
32 advances our understanding of how various model types, each with distinct mechanisms, can  
33 be effectively leveraged alongside multi-source datasets across diverse scenarios.

34

35 **Highlights**

36 • Combining LSTM and  $\delta$ HBV with diverse forcings sets new accuracy benchmarks  
37 • Ensembling models with one forcing outperforms merging forcings as an input  
38 •  $\delta$ HBV and LSTM together always increase NSEs, especially spatial generalization  
39 •  $\delta$ HBV provides valuable spatial constraints in the deterministic ensemble simulations  
40 •  $\delta$ HBV and LSTM have different error characteristics that can be offset in an ensemble

41

42 **Keywords**

43 Streamflow simulation, differentiable model, deep learning, hybrid modeling, multi-source  
44 fusion

45

46 **1. Introduction**

47 Streamflow, a critical component of the global hydrosphere, profoundly influences both  
48 human society and natural ecosystems (Lins and Slack, 1999). Accurate simulation and  
49 prediction of streamflow yield numerous benefits, including improved flood prevention  
50 strategies (Brunner et al., 2021). Hydrological models serve as indispensable tools for  
51 achieving this objective and can be traditionally categorized into two types: data-driven models  
52 (Feng et al., 2020; Kratzert et al., 2018; Liu et al., 2024; Nearing et al., 2024) and process-  
53 based (or physically-based) models (Newman et al., 2017; Paul et al., 2021). Data-driven  
54 models, exemplified by long short-term memory (LSTM) (Feng et al., 2020; Kratzert et al.,  
55 2018) and transformer (Liu et al., 2024) networks, excel in learning patterns from multi-source  
56 data (Li et al., 2023b, 2024; Liu et al., 2022; Nearing et al., 2024) and generally achieve high  
57 performance. However, they often lack interpretability and may not resolve extreme values  
58 very well (Li et al., 2020a; Song et al., 2025b). Conversely, process-based models, derived

59 deductively from physical laws or conceptualized views of natural systems, offer insights into  
60 internal hydrological processes but may exhibit weaker performance due to structural  
61 inadequacies (Li et al., 2020a, [2022](#); Zhang et al., 2019).

62 To combine the benefits and counteract the weaknesses of these two kinds of models,  
63 many efforts have been made to incorporate physical constraints and structures into data-driven  
64 models to align with fundamental physical principles, such as mass and water balances (Bandai  
65 and Ghezzehei, 2021; Wang et al., 2020; Xie et al., 2021). The most seamless integration uses  
66 neural networks to provide parameterizations or missing process representations for process-  
67 based models (Aboelyazeed et al., 2023; Bindas et al., 2024; Feng et al., 2022; Jiang et al.,  
68 2020; Kraft et al., 2022; Rahmani et al., 2023; Song et al., 2024b; Tsai et al., 2021). These  
69 differentiable models (Shen et al., 2023) connect (flexible amounts of) prior physical  
70 knowledge to neural networks, and have displayed many advantages, including improved  
71 computational efficiency and prediction of untrained variables (Tsai et al., 2021), spatial  
72 generalization (Feng et al., 2023b), and representation of extremes (Song et al., 2025b).  
73 However, it is also unclear whether current differentiable models, e.g.,  $\delta$ HBV, the  
74 Hydrologiska Byråns Vattenbalansavdelning (HBV) model implemented within a  
75 differentiable framework (Feng et al., 2023b; [Ji et al., 2025](#); Shen et al., 2023; Song et al.,  
76 2025b), have unique bias characteristics that are associated with the process-based parts of their  
77 structures that cannot be reduced once the equations are prescribed.

78 Orthogonal to such efforts are ensemble simulations (Yu et al., 2024), which combine  
79 many members with different biases and uncertainties to mitigate their respective biases in  
80 deterministic predictions. Many previous studies have tried ensemble methods to improve  
81 streamflow (Clark et al., 2016; Zounemat-Kermani et al., 2021) based on many factors, like  
82 initial conditions (e.g., initial weights and biases in LSTM (Kratzert et al., 2018)), data used  
83 for parameterization (Feng et al., 2021), and objective functions (Lin et al., 2024). These

84 studies generally use one model to generate the differences among the ensemble members.  
85 Furthermore, some studies (Dion et al., 2021; Solanki et al., 2025) have utilized simulations  
86 from multiple different models but are limited to process-based models, resulting in ensemble  
87 simulations that are better than each individual member. Thus far, however, most studies have  
88 focused on simulations from only similar models or model types, and little work has tested an  
89 ensemble across the boundary of model types, particularly between data-driven, process-based,  
90 and hybrid models, especially on a large number of samples. Presumably, if each model has its  
91 own unique bias, data-driven and process-based models are likely to exhibit greater differences  
92 due to their inherently distinct characteristics. It remains unclear whether ensembling across  
93 model types should bring benefits to deterministic predictions. Furthermore, grounded in the  
94 process-based model, the differentiable process-based hydrological model, such as  $\delta$ HBV,  
95 significantly enhances performance compared to traditional process-based models, while on  
96 the other hand introducing greater uncertainty regarding its potential benefits when ensembled.  
97 Moreover, previous studies have primarily focused on evaluating ensemble simulations for  
98 temporal predictions. However, streamflow simulation under spatial extrapolation scenarios  
99 presents greater challenges, and findings from temporal tests may not be directly applicable in  
100 this context.

101 It is known that the performance of any type of hydrologic model heavily depends on the  
102 quality of input data, particularly meteorological forcing data (Bell and Moore, 2000; Yao et  
103 al., 2020), and other inputs, like the uncertainties of initial conditions, can be mitigated via  
104 warming up (Yu et al., 2019). While independent forcing datasets excel in certain aspects, they  
105 each carry different error characteristics (Beck et al., 2017; Behnke et al., 2016; Newman et al.,  
106 2019) and accordingly affect the hydrological models in different ways. In order to fully display  
107 the different features between LSTM and  $\delta$ HBV, multiple forcing datasets could be considered.  
108 Given the utilization of multiple forcing datasets, one could choose to use data fusion to

109 combine them into a single coherent model input (Kratzert et al., 2021; Sawadekar et al., 2025),  
110 or to pass each forcing dataset through a model and then afterwards combine the multiple  
111 outputs in an ensemble. It is not clear which approach is more beneficial.

112 Considering the knowledge gaps discussed above, we sought to answer several research  
113 questions:

- 114 1. Will a cross-model-type ensemble of LSTM and  $\delta$ HBV improve deterministic  
115 streamflow prediction more than a within-class ensemble?
- 116 2. Is it better to use multiple forcings in one model or to ensemble multiple models, each  
117 with a different forcing input?
- 118 3. Do process-based equations bring unique value to an ensemble, especially in terms of  
119 spatial generalizability?

120 The remainder of this paper is structured as follows: Sect. 2 outlines the hydrological data  
121 and models used in this study, as well as the experimental design. Results and discussions are  
122 presented in Sect. 3, with conclusions provided in Sect. 4.

123

## 124 **2. Materials and methods**

### 125 2.1. CAMELS hydrologic dataset

126 The Catchment Attributes and Meteorology for Large-sample Studies (CAMELS) dataset  
127 (Addor et al., 2017) is widely employed for hydrological model evaluation and community  
128 benchmarking. The CAMELS dataset encompasses 671 basins distributed across the  
129 conterminous United States, with basin sizes ranging from 1 to 25,800 km<sup>2</sup> (median: 335 km<sup>2</sup>).  
130 This standardized and publicly available dataset serves as a benchmark for evaluating various  
131 hydrological models, with LSTM models trained on this dataset often serving as a reference  
132 point for comparing other models (Kratzert et al., 2021). CAMELS provides basin-scale data,  
133 including streamflow observations and static basin attributes, as well as forcing datasets from

134 three independent sources: Daymet (Thornton et al., 1997), North American Land Data  
135 Assimilation System (NLDAS) (Xia et al., 2012), and Maurer (Maurer et al., 2002). Each of  
136 the three meteorological forcing datasets operates at a daily temporal resolution, encompassing  
137 precipitation, temperature, vapor pressure, and surface radiation variables, with daily  
138 temperature extrema of NLDAS and Maurer supplemented from Kratzert et al. (2021). These  
139 three meteorological forcing datasets have methodological distinctions in spatial resolution,  
140 data generation approaches, and temporal processing (Behnke et al., 2016; Kratzert et al., 2021).  
141 Exemplary plots illustrating the differences among the three meteorological forcing datasets  
142 are provided in Appendix B. These features can lead to dataset-specific error characteristics  
143 and make them valuable for displaying the distinct features of different model types. All model  
144 inputs used in this study are detailed in Table C1.

145

146 2.2. Long short-term memory

147 As one kind of deep learning algorithm, long short-term memory (LSTM) (Hochreiter and  
148 Schmidhuber, 1997) has unique structures like hidden states and gates activated by the tanh  
149 and sigmoid functions (Li et al., 2023a), respectively. These features enable LSTM to excel in  
150 streamflow simulation tasks (Feng et al., 2020; Kratzert et al., 2018; Nearing et al., 2024). In  
151 the current benchmark framework, LSTM models are trained using dynamic atmospheric  
152 forcings and static basin attributes as inputs, with streamflow as the target output, making it  
153 perform well in both temporal and spatial tests (Figure 1a). In this work, for cross-group  
154 comparability, we used the LSTM model and its hyperparameters as reported in Kratzert et al.  
155 (2021).

156

157 2.3. Differentiable HBV model ( $\delta$ HBV)

158 The Hydrologiska Byråns Vattenbalansavdelning (HBV) model is a parsimonious bucket-

159 type hydrologic model that simulates various hydrological variables, including snow water  
160 equivalent, soil water, groundwater storage, evapotranspiration, quick flow, baseflow, and total  
161 streamflow (Aghakouchak and Habib, 2010; Beck et al., 2020; Bergström, 1976, 1992).  
162 Recently demonstrated differentiable HBV ( $\delta$ HBV) model (Feng et al., 2023b; [Ji et al., 2025](#);  
163 Shen et al., 2023; Song et al., 2024b) incorporates deep neural networks for both regionalized  
164 parameterization and missing process representations within a differentiable programming  
165 framework that supports “end-to-end” training (Figure 1b). This innovation enables  $\delta$ HBV to  
166 effectively learn from data while obeying physical laws, resulting in high-level performance  
167 for streamflow simulations. From the perspective of process-based modeling, LSTM is a  
168 regionalized parameter provider that leverages the autocorrelated nature of its inputs to impose  
169 an implicit spatial constraint on the generated parameters.

170 In this study, we used  $\delta$ HBV1.1p (Song et al., 2024b, 2025b), which is an updated version  
171 of  $\delta$ HBV1.0 (Feng et al., 2022, 2023b). The main improvement is the addition of a capillary  
172 rise module, which enhances the characterization of low flows. [Other modifications include](#)  
173 [three additional](#) modifications [are included](#) to address high-flow simulation challenges: the  
174 use of three dynamic parameters ( $\gamma, \beta, k_0$ ) (Song et al., 2025b); the removal of log-transform  
175 normalization for precipitation; and the adoption of the normalized squared-error loss function  
176 ([Table C2](#)) (Frame et al., 2022; Kratzert et al., 2021; Song et al., 2025a, b; Wilbrand et al.,  
177 2023). We also maintain dynamic parameters during warm-up periods. Although this provides  
178 only marginal benefits and increases computational costs, it yields a more realistic  
179 representation and reduces uncertainties associated with initial conditions. The basic equations  
180 in  $\delta$ HBV are as follows:

$$\theta = LSTM_w(\bar{x}, \bar{A}_{attr}) \quad (1)$$

$$Q = HBV(x, \theta) \quad (2)$$

$$W_{opt} = \operatorname{argmin}_w (L(Q, Q^*)) \quad (3)$$

181 where  $\theta$  are the dynamic or static physical parameters,  $w$  denotes the weights and biases of  
182 LSTM,  $x$  includes the basin-averaged meteorological forcings, such as precipitation, mean  
183 temperature, and potential evapotranspiration, with  $\bar{x}$  representing their normalized versions.  
184 Similarly,  $\bar{A}_{attr}$  consists of normalized observable basin-averaged attributes, encompassing  
185 basin area, topography, climate, soil texture, land cover, and geology (Table C1). Precipitation  
186 and mean temperature are from CAMELS, while potential evapotranspiration is calculated  
187 ~~based on using~~ the Hargreaves (1994)(1994) method ~~using mean, based on~~ maximum, and  
188 minimum temperatures along with basin latitudes, all from data described in sect. 2.1.  $Q$  and  
189  $Q^*$  are the streamflow simulations (model outputs) and observations (as provided in CAMELS),  
190 respectively. HBV is implemented on PyTorch so it is programmatically differentiable: all  
191 steps store information related to gradient calculations during backpropagation, allowing this  
192 model to be trained together with neural networks in an end-to-end fashion. More details about  
193 differentiable HBV can be found in previous studies (Feng et al., 2022; Song et al.,  
194 2024b)(Feng et al., 2022; Song et al., 2024b). The details of some particularly relevant HBV  
195 processes are described in Appendix A.

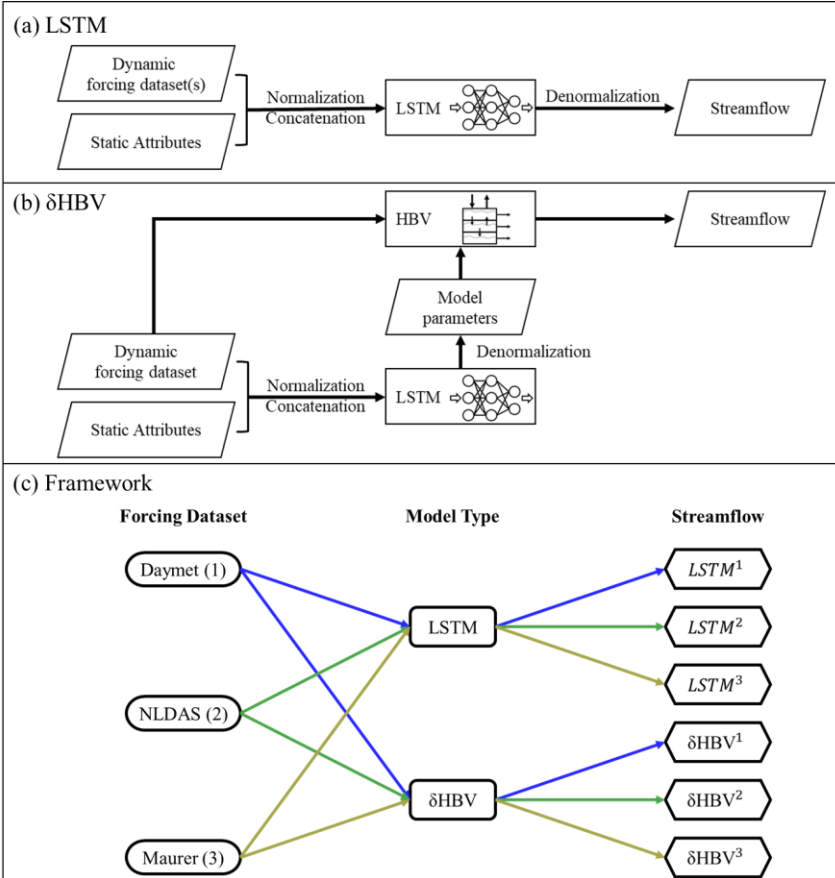
196

#### 197 2.4. Experimental design

198 In this study, we trained the two models of very different types (LSTM and  $\delta$ HBV), each  
199 with one of three meteorological forcing datasets (Daymet, NLDAS, and Maurer), resulting in  
200 six corresponding streamflow simulations (Figure 1c) for each different test scenario (see sect.  
201 2.5 for additional information). The training processes of LSTM and  $\delta$ HBV followed Kratzert  
202 et al. (2021)(2021) and Feng et al. (2023b)(2023b), respectively. Test results and performance  
203 metrics for all models are reported for the 531-basin subset that excludes those with areas larger  
204 than 2,000 km<sup>2</sup> or with more than a 10% discrepancy between different basin area calculation

205 methods ([Newman et al., 2017](#))[\(Newman et al., 2017\)](#).

206 To generate ensembles, we tested various weighting strategies and ultimately employed  
207 averaging to combine the six single-forcing, single-model-type simulations, as it yielded the  
208 best performance. To better describe various combinations including cross-model ensembles,  
209 these simulations were categorized into six groups (Table 1). A shorthand notation is used  
210 throughout the remainder of this work to describe the forcing datasets and ensembles. Daymet,  
211 NLDAS, and Maurer are abbreviated as superscripts 1, 2, and 3, respectively. The + symbol is  
212 used to group model types being ensembled, while superscript clustering (e.g., <sup>12</sup> or <sup>123</sup>) is used  
213 to group the meteorological forcing types being ensembled, with parentheses indicating that  
214 the superscripts apply to all model types within. For example,  $(LSTM + \delta HBV)^{123}$  could be  
215 explicitly written as  $LSTM^1 + LSTM^2 + LSTM^3 + \delta HBV^1 + \delta HBV^2 + \delta HBV^3$ . To compare  
216 two different strategies to utilize the multiple meteorological forcing datasets and to benchmark  
217 against the previously highest performance, we additionally trained a single LSTM model using  
218 all three forcing datasets as simultaneous inputs as done by Kratzert et al. ([\(2021\)](#)[\(2021\)](#)),  
219 referred to as LSTM<sup>multi</sup> (the last row in Table 1).



220

221 *Figure 1. (a) The LSTM structure, (b) the  $\delta$ HBV structure, and (c) the framework to generate*  
 222 *the six individual ensemble members of the streamflow simulations, in which different colors*  
 223 *of arrow lines denote the different meteorological forcing datasets (also denoted as 1, 2, 3),*  
 224 *respectively.*

225 *Table 1. (a) The six groups of streamflow simulations, and (b) the streamflow simulation via*  
 226 *LSTM based on a different strategy, in which three meteorological forcing datasets were*  
 227 *combined as a single set of inputs (Kratzert et al., 2021) (Kratzert et al., 2021). Superscripts 1,*  
 228 *2, and 3 denote Daymet, NLDAS, and Maurer, respectively. The ensemble across forcings*  
 229 *("ef") superscript indicates an ensemble of model simulations, each of which uses a different*  
 230 *single meteorological forcing, e.g.,  $LSTM^{12}$  means the average of  $LSTM^1$  and  $LSTM^2$ .*

<b>(a) Six Groups of Streamflow Simulations</b>		
<b>Group Name</b>	<b>Group Members</b>	
LSTM	$LSTM^1, LSTM^2, LSTM^3$	
$\delta HBV$	$\delta HBV^1, \delta HBV^2, \delta HBV^3$	
$LSTM + \delta HBV$	$(LSTM + \delta HBV)^1, (LSTM + \delta HBV)^2, (LSTM + \delta HBV)^3$	
$LSTM^{ef}$	$LSTM^{12}, LSTM^{13}, LSTM^{23}, LSTM^{123}$	
$\delta HBV^{ef}$	$\delta HBV^{12}, \delta HBV^{13}, \delta HBV^{23}, \delta HBV^{123},$	
$(LSTM + \delta HBV)^{ef}$	$(LSTM + \delta HBV)^{12}, (LSTM + \delta HBV)^{13}, (LSTM + \delta HBV)^{23},$ $(LSTM + \delta HBV)^{123}$	
<b>(b) Using forcing datasets as simultaneous inputs to an LSTM</b>		
<b>Streamflow Simulation</b>	<b>Model Type</b>	<b>Meteorological Forcing Dataset</b>
$LSTM^{multi}$	LSTM	Daymet, NLDAS, Maurer

231  
 232

233 2.5. Evaluation scenarios and criteria

234 The above cases were comprehensively evaluated for performance in temporal  
235 extrapolation (Feng et al., 2022; Kratzert et al., 2018)(Feng et al., 2022; Kratzert et al., 2018),  
236 as well as two types of spatial generalization: prediction in ungauged basins (PUB) (Feng et  
237 al., 2023b; Kratzert et al., 2019)(Feng et al., 2023b; Kratzert et al., 2019), and prediction in  
238 ungauged regions (PUR) (Feng et al., 2021, 2023b):

Field Code Changed

239 • **Temporal Test:** Models were trained using data from all basins and tested across  
240 different periods.

241 • **PUB Test:** Models were trained on randomly selected subsets from all basins and  
242 tested on the remaining basins during the same time period.

243 • **PUR Test:** Different from the PUB test, basins were grouped into continuous regions,  
244 one of which was selected to comprise the group of testing basins while the others  
245 were used for training.

246 Temporal generalization is generally considered to be the easiest of these tests. In terms  
247 of spatial generalization, which approximates data-sparse scenarios, the PUB test is an example  
248 of spatial interpolation, whereas the PUR test involves spatial extrapolation. The PUR test is  
249 widely regarded as the most challenging and may therefore produce findings that differ  
250 significantly from those in other scenarios. In this study, all basins were divided into 10  
251 spatially stratified groups for the PUB test and 7 fully disjoint regional groups for the PUR test  
252 (Table 2) in the same way as Feng et al. (2023b)(2023b). The spatial extent of the 7 regions for  
253 the PUR test is also shown in Figure 3(c1-c2). Therefore, we conducted 10 rounds for the PUB  
254 test and 7 rounds for the PUR test, with a different group held out for testing in each round.  
255 Model performance was evaluated after concatenating the test results for all basins.

256

257 *Table 2. Differences of temporal, PUB, and PUR tests.*

Test Scenario	Training		Testing	
	Basin	Time	Basin	Time
Temporal	All <sup>a</sup>	1980-1995 <sup>b</sup>	All	1995-2010
PUB	Random nine-tenths	1980-1999	Holdout <sup>c</sup>	1995-1999
PUR	Random six of seven regions	1980-1999	Holdout	1995-1999

258 <sup>a</sup>*δHBV training followed Feng et al. (2023b)(2023b) using all 671 CAMELS basins, while*  
 259 *LSTM training followed Kratzert et al (2021)(2021) using the selected 531-basin subset. Test*  
 260 *results and performance metrics for all models are reported for the 531 basins.*

261 <sup>b</sup>*Each hydrological year spans from October 1st to September 30th of the following year.*

262 <sup>c</sup>*In the PUB and PUR tests, models are run for 10 and 7 rounds, respectively, with the group*  
 263 *held out for testing changed in each round. The simulation performance was evaluated after*  
 264 *concatenating the test results for all basins.*

265

266 We repeated all the simulations with three different random seeds. Therefore, all the  
 267 simulations come from a total of  $(2 \times 3 + 1) \times (1 + 10 + 7) \times 3$  trained models. The first factor  
 268 represents the models: two model types (LSTM and δHBV) trained separately with each of the  
 269 three forcing datasets, along with *LSTM<sup>multi</sup>*, a single model instance trained using all three  
 270 forcing datasets simultaneously. The second factor accounts for the three types of tests  
 271 (temporal, PUB, and PUR tests), and the last for the three random seeds. With respect to  
 272 random seeds, we present two variations in the results, which are visually depicted in Figure  
 273 C1. The results without “seed” as a subscript represent the average metric values from multiple  
 274 streamflow simulations, each generated from a single model implementation, along with the  
 275 corresponding uncertainties, visualized using error bars. The results marked with “seed” as a  
 276 subscript are based on the average of multiple streamflow simulations conducted with different  
 277 random seeds. In terms of computational cost, training LSTM (30 epochs) and δHBV (50  
 278 epochs) for temporal testing under a single meteorological forcing dataset takes approximately

279 5 and 21 hours, respectively, using a single NVIDIA Tesla V100 GPU.

280 We calculated several well-established performance metrics: Nash-Sutcliffe model  
281 efficiency coefficient (NSE) ([Nash and Sutcliffe, 1970](#)) ([Nash and Sutcliffe, 1970](#)), Kling-  
282 Gupta model efficiency coefficient (KGE) ([Kling et al., 2012](#)) ([Kling et al., 2012](#)), percent bias  
283 (*PBIAS*), and root-mean-square error (*RMSE*). We also considered *RMSE* values for high (top  
284 2% “peak” flow, *highRMSE*), low (bottom 30% “low” flow, *lowRMSE*), and mid-range (the  
285 remaining flow, *midRMSE*) flow conditions ([Yilmaz et al., 2008](#)) ([Yilmaz et al., 2008](#)). These  
286 metrics were computed for each basin and aggregated into error bars and cumulative density  
287 functions (CDFs). For brevity, the main text primarily reports NSE values, and other metric  
288 values are provided in Appendices D and E. Furthermore, we use the spread values ([Li et al.,](#)  
289 [2021; Reichle and Koster, 2003](#)) ([Li et al., 2021; Reichle and Koster, 2003](#)) to investigate  
290 ensemble variability and explore model complementarity. Detailed descriptions of these  
291 metrics and their calculations are available in Table C2.

292

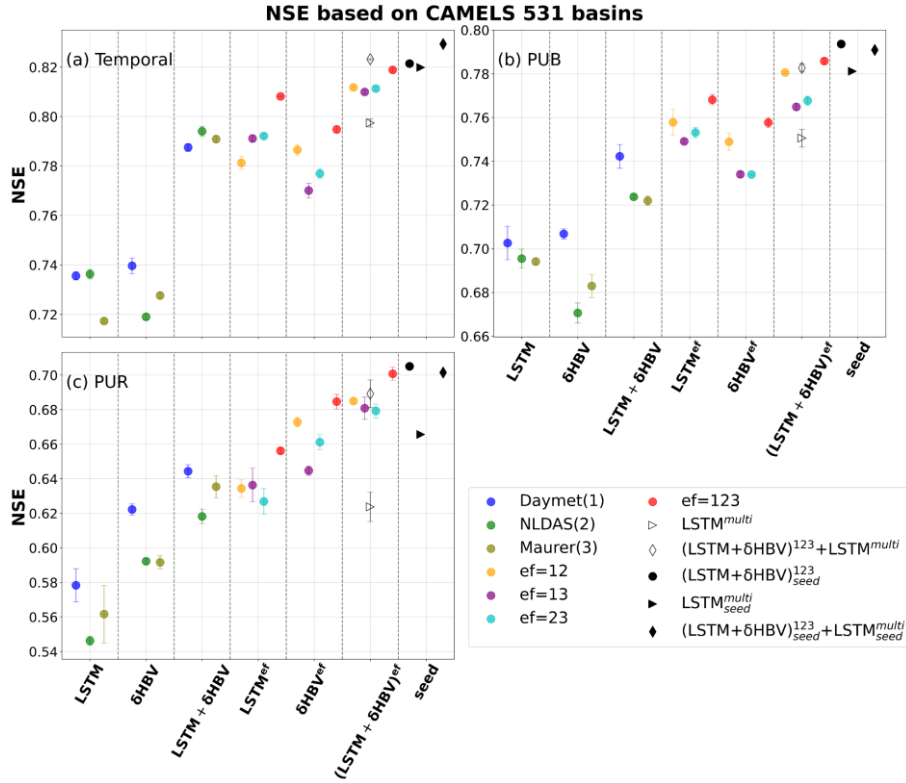
### 293 **3. Results and discussion**

#### 294 3.1. Temporal extrapolation

295 For the temporal test, in which models were trained and tested on the same basins but in  
296 different time periods, we found that cross-model-type ensembles noticeably surpassed the  
297 within-class ensembles when other conditions were the same, with small uncertainties as shown  
298 by the error bars in Figure 2. With a single forcing dataset, the median NSE was elevated from  
299  $\sim 0.735$  for LSTM to  $\sim 0.79$  with  $\delta$ HBV added, though  $\delta$ HBV performance was similar to LSTM  
300 ( $\sim 0.74$  under Daymet). Even after LSTM achieved very high performance when its simulations,  
301 each derived separately from different meteorological forcing datasets, were ensembled ( $ef =$   
302 123,  $\sim 0.808$ ), adding  $\delta$ HBV still improved the results to  $\sim 0.818$ . This finding was robust for  
303 all different combinations of the tested meteorological forcing datasets. Conversely, adding

304 LSTM also helped to improve  $\delta$ HBV ensembles. These results highlight the benefits of the  
305 cross-model-type ensemble framework and indicate distinct simulation features for each model  
306 type. LSTM is a data-driven method that has low bias and large variance. [Data errors \(Li et al., 2020b\)](#)  
307 [Data errors \(Li et al., 2020b\)](#), different sampling strategies [\(Nai et al., 2024\)](#)[\(Nai et al., 2024\)](#), or even different weight initializations [\(Narkhede et al., 2022\)](#)[\(Narkhede et al., 2022\)](#)  
308 can lead to substantively different outcomes. Conversely,  $\delta$ HBV may have a smaller variance  
309 but a larger bias due to the fixed HBV formulation [\(Moges et al., 2016\)](#)[\(Moges et al., 2016\)](#) for  
310 some scenarios like low flows [\(Feng et al., 2023b; Song et al., 2024b\)](#)[\(Feng et al., 2023b; Song et al., 2024b\)](#) or in basins with significant water uses [\(Song et al., 2024a\)](#)[\(Song et al., 2024a\)](#).  
311 These errors with varying characteristics from different model classes can partially offset each  
312 other in an ensemble. On a side note,  $\delta$ HBV models seem more reliant on the quality of the  
313 forcing data, as shown in Figure 2.  $\delta$ HBV with the Maurer and NLDAS forcing datasets  
314 generally performs worse than it does with Daymet, which has lower biases. However, even in  
315 those cases, the combination of LSTM and  $\delta$ HBV was still better than LSTM alone, attesting  
316 to the robustness of these benefits.  
317  
318

319  
320



321

322 *Figure 2. Median NSE values for 531 CAMELS basins, indicating model and ensemble*

323 *performances for (a) temporal, (b) prediction in ungauged basin (PUB), and (c) prediction in*

324 *ungauged region (PUR) tests. Different simulations are represented by variously-shaped and*

325 *-colored points, and are organized by ensemble group, listed along the x-axis: LSTM,  $\delta\text{HBV}$ ,*

326  *$\text{LSTM}+\delta\text{HBV}$ , and their “ensemble forcing” counterparts,  $\text{LSTM}^{\text{ef}}$ ,  $\delta\text{HBV}^{\text{ef}}$ , and  $(\text{LSTM} +$*

327  $\delta\text{HBV})^{\text{ef}}$ .  $\text{LSTM}^{\text{multi}}$  is a single LSTM model trained directly on all three forcing datasets at

328 *once. The superscript “ef” denotes the forcing datasets involved in each ensemble (choices of*

329 *1 for Daymet, 2 for NLDAS, and 3 for Maurer), while the “+” connects the model types used*

330 *within an ensemble. The x-axis group and subscript “seed” indicate that simulation results*

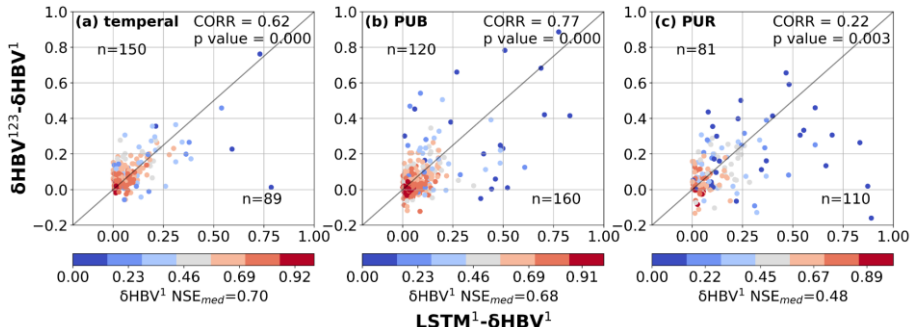
331 *were averaged based on three different random seeds (see Figure C1). Other points without*

332 *“seed”, along with their corresponding error bars, are derived from the averages of metrics*

333 *computed over repeated runs with three different random seeds. The error bar indicates one*

334 *standard deviation above and below the average value for each simulation.*

335



336

337 *Figure 3. Scatter plots comparing the performance differences between hydrological models*  
 338 *for the basins where LSTM outperformed δHBV (the basins where δHBV outperformed are not*  
 339 *shown in this plot). The x-axis represents the NSE differences between LSTM<sup>1</sup> and δHBV<sup>1</sup>*  
 340 *(LSTM<sup>1</sup> - δHBV<sup>1</sup>), while the y-axis shows the NSE differences between δHBV<sup>123</sup> and δHBV<sup>1</sup>*  
 341 *(δHBV<sup>123</sup> - δHBV<sup>1</sup>). Points are color-coded according to the NSE values of δHBV<sup>1</sup>. The*  
 342 *correlation coefficient (CORR) and p values between the x-axis values and the y-axis values,*  
 343 *along with the median NSE value of δHBV<sup>1</sup> (NSE<sub>med</sub>) on these basins, are also noted. We*  
 344 *note that NSE is not additive and should generally not be subtracted. Here the purpose is only*  
 345 *to confirm that basins where LSTM outperforms δHBV also tend to be those that benefit from*  
 346 *the ensemble of forcings.*

347

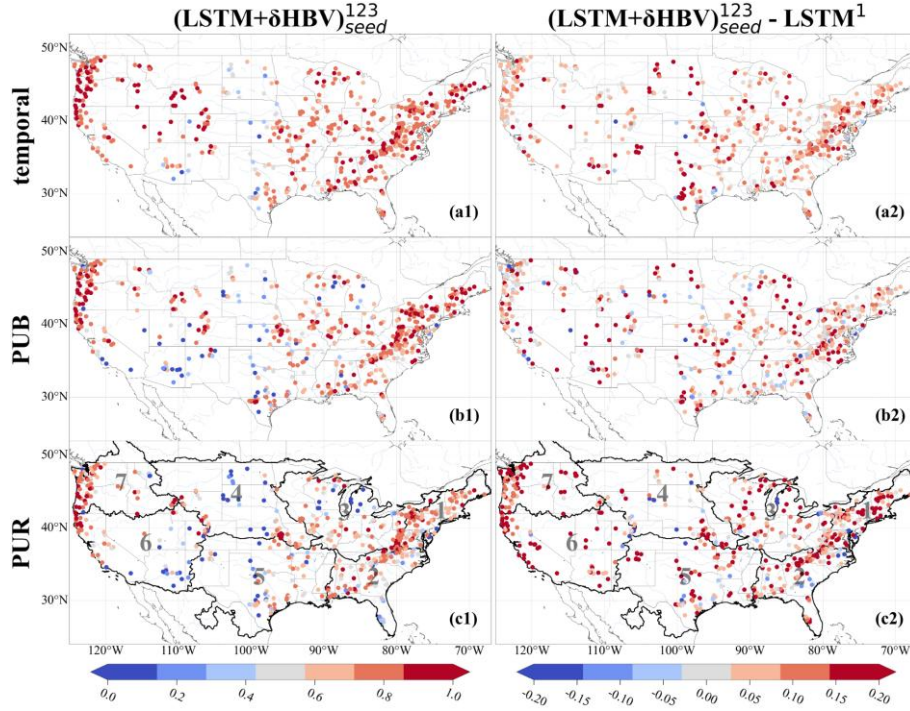
348 In the lower-performing basins where LSTM<sup>1</sup> had advantages over δHBV<sup>1</sup>, the ensemble  
 349 of meteorological forcings δHBV<sup>123</sup> also tended to be higher than δHBV<sup>1</sup> (Figure 3),  
 350 suggesting that forcing quality was a significant reason behind the underperformance of δHBV<sup>1</sup>  
 351 in these basins. Similar patterns were also observed when analyzing δHBV<sup>2</sup> and δHBV<sup>3</sup> values  
 352 (Figure D1 and Figure D2). These basins previously contributed to LSTM's cumulative  
 353 distribution function of NSE diverging from that of δHBV<sup>1</sup> at the low end (Feng et al., 2022).  
 354 Forcing errors can exist in the form of systematic timing errors, low or high bias for larger  
 355 events, etc., which can be difficult for the mass-balanced conceptual HBV<sup>1</sup> structure to adapt  
 356 to these errors. Because the ensemble of forcings tends to suppress the errors in each forcing  
 357 source, part of the advantages of δHBV<sup>123</sup> over δHBV<sup>1</sup> can be attributed to reducing forcing  
 358 bias or timing errors. Since the advantages of LSTM<sup>1</sup> over δHBV<sup>1</sup> also tend to occur with these

359 same basins, this also explains how LSTM<sup>1</sup> surpasses  $\delta$ HBV<sup>1</sup> in some basins with poorer-  
360 quality forcings. In contrast to  $\delta$ HBV, LSTM has the innate ability to shift information in time  
361 and moderately adjust the input scale. Moving from temporal validation to PUB to PUR  
362 scenarios, the advantages of diverse forcing datasets appear to diminish, as evidenced by the  
363 decreasing ratio of points above versus below the diagonal line, since the forcing error patterns  
364 remembered by LSTM may not generalize well in space (discussed in more detail in sect. 3.2).

365

366 Ensembling streamflow simulations from different meteorological forcing datasets  
367 demonstrates certain advantages over the previous approach of simultaneously sending  
368 multiple forcings into a data-driven model like LSTM ([Kratzert et al., 2021](#))[\(Kratzert et al.,](#)  
369 [2021\)](#). Ensembling LSTM simulations each using a single forcing dataset ( $LSTM^{123}$ ) resulted  
370 in an NSE value of 0.8082, higher than that of 0.7974 from feeding multiple forcing datasets  
371 into a single LSTM ( $LSTM^{multi}$ ). This difference was more pronounced in the cross-model-  
372 type ensemble, after including  $\delta$ HBV, compared to the previous within-class ensemble, and  
373 particularly notable for the spatial generalization tests (to be discussed in more detail in Sect.  
374 3.2), with). The corresponding specific metric values performance metrics are summarized in  
375 Tables D1–D5, with seasonal evaluations provided in Tables D1–D5Figure D3. These results  
376 indicate that the trained LSTM in  $LSTM^{multi}$  may be overfitted to the significant redundant  
377 information in these three forcing datasets, and that only LSTM models alone cannot fully  
378 exploit the information hidden in the multiple forcing datasets. Training separate ensemble  
379 members via different nonlinear hydrological processes, on the other hand, seems to allow  
380 different bias features to emerge with separate forcing datasets, accordingly mitigating them  
381 during the subsequent ensembling process.

382

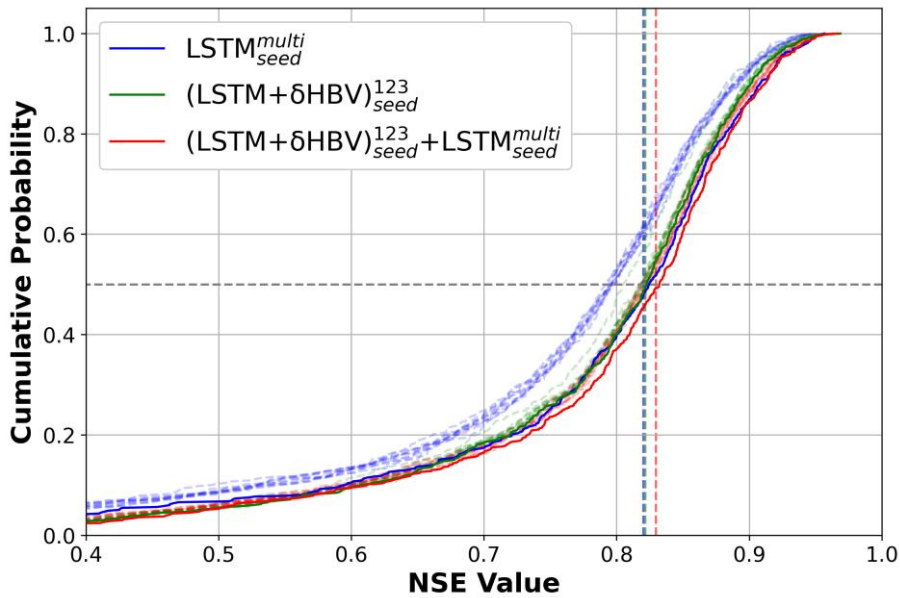
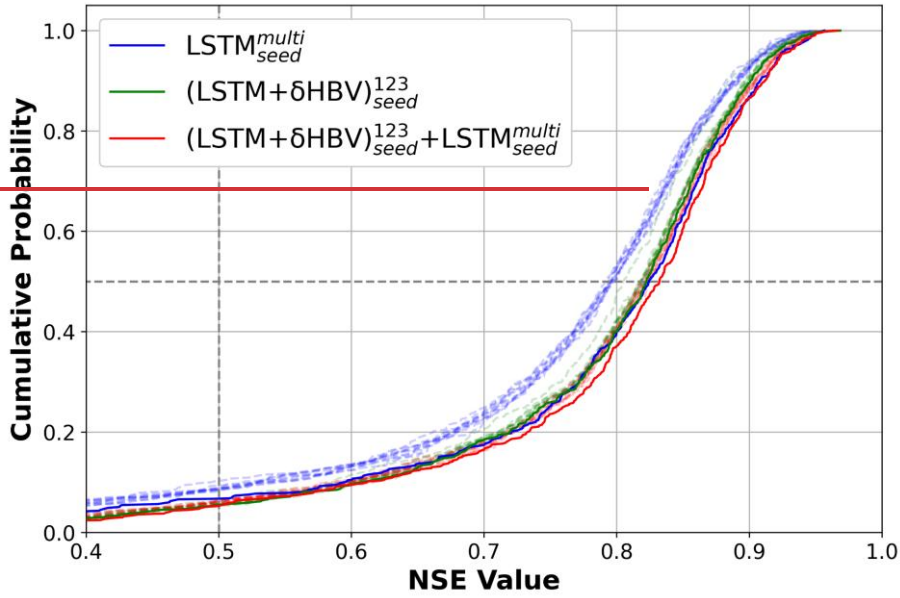


383 *Figure 4. Spatial distributions of NSE values over 531 basins. Subplots are arranged in rows, 384 indicating (a) temporal, (b) PUB, and (c) PUR test results, and columns, denoting (1) NSE 385 values from  $(LSTM + \delta HBV)_{seed}^{123}$  and (2) the differences between these NSE values and those 386 of  $LSTM^1$  (models using only forcing 1, Daymet). For  $LSTM^1$ , each NSE value reported was 387 the average of three NSE values from three simulations using three different random seeds. 388 The seven continuous regions used to divide up basins for the PUR test are outlined and 389 numbered in the PUR test maps.*

391  
392 Our most diverse ensemble,  $(LSTM + \delta HBV)_{seed}^{123} + LSTM_{seed}^{multi}$ , achieved a median NSE  
393 value of  $\sim 0.83$ , surpassing the  $\sim 0.82$  benchmark set by  $LSTM_{seed}^{multi}$  (Table D4). This  
394 advancement was achieved through random seed variation and cross-model-type ensembling.  
395 The performance of  $(LSTM + \delta HBV)_{seed}^{123}$  ensemble proved more robust than  $LSTM_{seed}^{multi}$ , with  
396 only a slight boost when we incorporated random seeds, i.e.,  $(LSTM + \delta HBV)_{seed}^{123}$ . Notably,  
397 the derived  $(LSTM + \delta HBV)_{seed}^{123}$  ensemble outperformed  $LSTM^1$  across almost all basins

398 (Figure 4). Further incorporation of  $LSTM^{multi}$  into this framework, especially when using  
399 multiple random seeds,  $(LSTM + \delta HBV)_{seed}^{123} + LSTM_{seed}^{multi}$ , yielded the best overall  
400 performance. Here, the margin over the previous benchmark was small in the temporal test.  
401 However, as we will show in sect. 3.2, the previous benchmark,  $LSTM_{seed}^{multi}$ , lacked robustness,  
402 exhibited greater deficiencies in spatial generalization, and negatively impacted ensemble  
403 simulations.

404 When we changed the number of random seeds from 3 to 10, we found that although all  
405 model and ensemble performances slightly increasedimproved, the gaps between them did not  
406 change much (Figure 5-and; Table D5 for 10 seeds, Table D4 for 3 seeds). In particular, the  
407 gap between  $(LSTM + \delta HBV)_{seed}^{123} + LSTM_{seed}^{multi}$  and  $(LSTM + \delta HBV)_{seed}^{123}$  or  $LSTM_{seed}^{multi}$   
408 remained unchanged. This indicates that the benefits from more random seeds rapidly become  
409 marginal, and our results based on 3 random seeds were sufficiently robust. For LSTMs alone,  
410 different random seeds displayed higher variation, and ensembling them led to greater  
411 improvement than ensembling  $(LSTM + \delta HBV)^{123}$  with additional random seeds. It was  
412 noteworthy that while the  $(LSTM + \delta HBV)^{123}$  ensemble generally showed the lowest RMSE  
413 values, it did not always show the best high flow performance, as indicated by highRMSE  
414 (Tables D1-D4). After incorporating the  $LSTM_{seed}^{multi}$  variant into  $(LSTM + \delta HBV)_{seed}^{123} +$   
415  $LSTM_{seed}^{multi}$ , overall RMSE and highRMSE both improved. Nevertheless, this ensemble did not  
416 always obtain the best values in other metrics like low flow (lowRMSE) and requires further  
417 improvement.  
418



421 *Figure 5. Cumulative distribution function (CDF) curves based on temporal test results for*  
 422  *$LSTM^{multi}$ ,  $(LSTM + \delta HBV)^{123}$ , and  $[(LSTM + \delta HBV)^{123} + LSTM^{multi}]$ . The solid lines*  
 423 *(with “seed”) denote the results with 10 random seeds while the corresponding dashed and*

424 translucent lines denote the performances of their individual members each based on one  
425 random seed. The median NSE values computed with 3 random seeds are also indicated by  
426 vertical dashed and translucent lines in the corresponding colors.

427

428 3.2. Spatial generalization

429 It is clear that cross-model-type ensembling and the incorporation of  $\delta$ HBV significantly  
430 improved prediction in ungauged basins (PUB) or regions (PUR), mitigating the difficulty of  
431 spatial generalization (Figure 2b - 2c). In particular, the previous record-holder for temporal  
432 test performance,  $LSTM_{seed}^{multi}$ , incurred large drops in the PUB and PUR tests, once again  
433 reminding us of the limitations of LSTM in spatial generalization. Given the same forcings,  
434  $\delta$ HBV-only individual simulations or ensembles consistently outperformed LSTM-only  
435 counterparts in the PUR test. Furthermore, adding  $\delta$ HBV to the same-model-type LSTM  
436 ensembles improved median NSE by 0.02-0.03 for PUB. The role of  $\delta$ HBV became even more  
437 prominent in the harder PUR tests, with an increased gap (0.04-0.07), e.g., LSTM<sup>123</sup> (median  
438 NSE ~0.656) and  $(LSTM + \delta HBV)^{123}$  (median NSE ~0.701). The increased significance of  
439  $\delta$ HBV is also illustrated by the optimized weights shown in Figure E1, which were estimated  
440 using a genetic algorithm with streamflow observations from the test periods. These weights  
441 are presented solely to illustrate the relative contributions of the different ensemble components.  
442 The significantly different spatial distribution patterns of these weights among different test  
443 scenarios also indicate the differences among temporal, PUB, and PUR tests (Figures E2-E3).

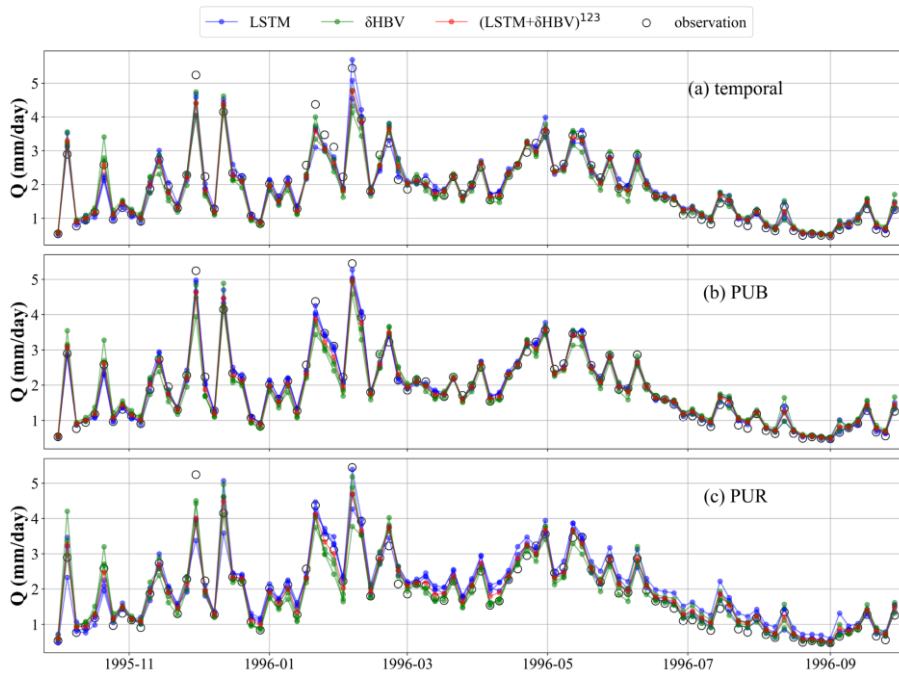
444 The performance of  $(LSTM + \delta HBV)^{123}$  improved compared to  $LSTM^{multi}$  regardless of  
445 whether or not we employed multiple random seeds were employed to form an ensemble. As  
446 such, we can conclude that the inclusion of a differentiable process-based model like  $\delta$ HBV in  
447 an ensemble is a systematic way to reduce the risks of failed generalizations of LSTM.

448 Utilizing a cross-model-type ensemble led to widespread improvements over LSTM-only  
449 ensembles, with the exception of a few scattered basins for each temporal (Figure 4-a2), PUB

450 (Figure 4-b2), and PUR (Figure 4-c2) test. The most significant improvements due to the  
451 ensemble were concentrated on the center of the Great Plains along with the midwestern US,  
452 while the eastern US was moderately improved, suggesting data uncertainty is a larger issue in  
453 the central and midwestern US. The Great Plains have historically had poor performance for  
454 all kinds of models ([Mai et al., 2022](#))[\(Mai et al., 2022\)](#) and even the ensemble model had NSE  
455 values of only 0.3-0.4 for many of the basins there, although this still marked significant  
456 improvements over LSTM<sup>1</sup> (Figure 4-a2, -b2, -c2). Some western basin NSE values were  
457 elevated by more than 0.15 for the temporal test (Figure 4-a2) and even more for PUB and  
458 PUR. Meteorological stations are generally sparse on the Great Plains, and an ensemble seems  
459 to be an effective way to leverage the different forcing datasets that are available. The poor  
460 performances in some basins highlight some remaining deficiencies in current models, which  
461 clearly cannot fully consider the heterogeneities of different basins; thus, multiscale  
462 formulations that resolve such heterogeneities may have advantages ([Song et al., 2024a](#))[\(Song](#)  
463 [et al., 2024a\).](#)

464 To investigate why ensembles outperformed single-model, single-forcing approaches, we  
465 compared their temporal, PUB, and PUR test simulation time series against observations for  
466 531 basins (Figure 6). Analysis of averaged hydrological year data revealed that while  
467 individual ensemble members using single-source forcing datasets performed similarly for  
468 easily simulated periods, they showed significant divergence during challenging periods,  
469 particularly peak flows. This divergence stems from distinct systematic errors inherent to  
470 different model types and forcing datasets. Notably, LSTM-based simulations alone proved  
471 insufficient in generating adequate spread to capture these divergent points. By averaging  
472 individual model outputs and stabilizing uncertainties, ensemble simulations achieved effective  
473 and robust performance across all conditions, which can be shown via the metric highRMSE  
474 and lowRMSE values in Tables D1-D4. This highlights the critical importance of

475 comprehensive training for each ensemble member, including diverse forcing inputs, full-  
 476 period model calibration, and rigorous hyperparameter tuning, to ensure that each member  
 477 develops distinct simulation behaviors. These differences allow the ensemble to better  
 478 represent a range of hydrological responses, particularly under extreme or uncertain conditions.  
 479 By capturing complementary strengths and compensating for individual weaknesses, such  
 480 well-trained ensemble members collectively enhance the robustness and accuracy of  
 481 streamflow simulations.

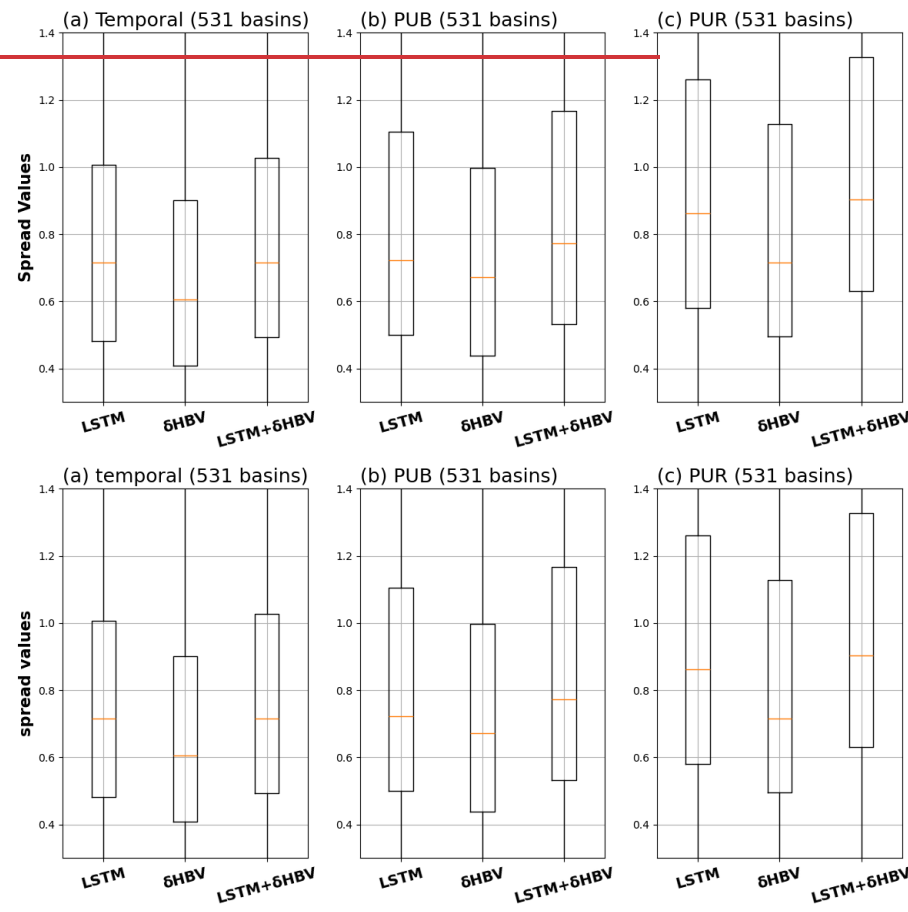


482  
 483 *Figure 6. Comparisons between multi-basin-averaged streamflow observations and*  
 484 *simulations across 531 basins. The time series points are displayed at four-day intervals for*  
 485 *clarity and conciseness. Ensemble members based on the same model (LSTM or δHBV) but*  
 486 *driven by different forcing datasets are shown in the same color to highlight the differences*  
 487 *between models more clearly.*

488  
 489 3.3 Ensemble variability and robustness analysis  
 490

Although δHBV (median spread 0.61) exhibits lower spreads than LSTM (mean spread

491 0.72), their combination increases the ensemble spreads, thereby enhancing diversity (Figure  
 492 7). This pattern holds across the temporal, PUB, and PUR tests. Ensemble effectiveness  
 493 depends on the diversity of model behaviors and their distinct error characteristics.  
 494 Consequently, larger spreads ~~contribute to~~ are generally associated with greater ensemble  
 495 benefits. Figure D3D4 further demonstrates that  $\delta$ HBV+LSTM exhibits larger spreads than  
 496 LSTM in most basins.



497  
 498  
 499 Figure 7. Spread values (Table C2) of each model for LSTM,  $\delta$ HBV, and LSTM +  $\delta$ HBV due  
 500 to different meteorological forcings and random seeds across temporal, PUB, and PUR tests.  
 501

502 As the warming signal is already clear across most basins under any forcing across the  
503 periods of simulation (Figure D4D5), the models' strong performance in the temporal test  
504 suggests decent extrapolation capability under warming scenarios. It is often questioned  
505 whether data-driven models like LSTM lose accuracy under stronger climate drift, but no  
506 substantially warmed dataset is available to test this. Benchmarks suggest LSTM captures 15-  
507 year trends well in temporal tests, but less so in data-sparse scenarios (Feng et al., 2023b)(Feng  
508 et al., 2023b). Introducing a 10% precipitation perturbation (multiplying precipitation by 1.1)  
509 slightly reduced performance for both models as expected (Figures D56a and D56b), but  
510 ensemble benefits remained robust across models despite the perturbation.

511 Training sample size, dynamic parameter choices, and lookback windows all have exerted  
512 only a limited impact on our conclusions. δHBV shows limited sensitivity to sample size, with  
513 similar results when trained on 531 versus 671 basins (Figure D56c). Regarding parameter  
514 uncertainties, fixing one δHBV parameter ( $k_0$ ) as static increased structural errors and reduced  
515 performance (Figure D56d), yet ensemble benefits remained robust. For LSTM, alternative  
516 window sizes of 182 and 730 days were tested, with the default 365-day window yielding  
517 optimal performance (Figure D56e). Importantly, variations in the lookback window had only  
518 minor effects on model performance, underscoring the robustness of ensemble benefits.

519  
520 3.4. Further discussion

521 Based on our results, we identified several avenues for future research. First, while we  
522 have explored various weighting strategies and found that averaging yields the best  
523 performance yet, we believe that dynamic or adaptive weighting schemes could further enhance  
524 performance in future studies. It is also demonstrated by Table E1 that estimated uneven  
525 weights can significantly improve simulation performance. Moreover, within specific basins,  
526 the estimated weights of different components are often highly imbalanced, as evidenced by  
527 the spatial distribution of optimized weights (Figures E2-E3). Some potential feasible ways

528 include using the simulations from these individually-trained models as inputs of a data-driven  
529 model (Solanki et al., 2025), and making the weight estimation and the ensemble member  
530 training simultaneously.

Field Code Changed

531 Both LSTM and  $\delta$ HBV models exhibit limitations in regions with significant  
532 anthropogenic impacts, such as like dam presence, as well as arid climatic and  
533 highly significantly heterogeneous geological conditions. These regions are mainly located in  
534 the midwestern and western CONUS, where high evaporation conditions (Heidari et al., 2020,  
535 Figure 2) and numerous dams (Ryan-Bellmore et al., 2017, Figure 1) coincide with complex  
536 water use processes (Wada et al., 2016, Figure 11) that current models cannot simulate well.  
537 Together, these factors suggest that anthropogenic influence is likely an important driver of  
538 poor model performance. Further improvements may include incorporating additional data that  
539 capture these factors like capacity-to-runoff ratio (Ouyang et al., 2021) or integrating  
540 specialized modules, such as reservoirs (Hanazaki et al., 2022; West et al., 2025). Compared  
541 with LSTM,  $\delta$ HBV is more sensitive to precipitation biases. For example, the differences  
542 between  $\delta$ HBV simulations under different forcing datasets were generally larger than those  
543 for LSTM, and  $\delta$ HBV using the Daymet forcing dataset showed largely better performance  
544 than with the other two forcing datasets, which indicates that  $\delta$ HBV may not be able to fit  
545 different forcing datasets well. Therefore, many potential structural optimizations can be  
546 implemented to improve  $\delta$ HBV. Our analysis provided corroborating evidence that forcing  
547 error is an important reason why LSTM can outperform  $\delta$ HBV in the temporal test for some  
548 basins, although such patterns may not generalize well in space. A meteorological forcing data  
549 correction module can be developed in the future to account for timing and magnitude errors  
550 in precipitation. Ensemble simulations may face challenges when computational resources are  
551 constrained, particularly for large-scale or real-time applications. Nevertheless, we remain  
552 optimistic about overcoming these challenges due to several promising solutions. These

553 include tailoring the hydrological model by simplifying less relevant components to specific  
554 simulation objectives (Clark et al., 2015; Kraft et al., 2022) and cloud-based computing  
555 infrastructures that offer scalable, on-demand resource allocation (He et al., 2024; Leube et al.,  
556 2013). Importantly, the majority of computational costs are incurred during model training. In  
557 practice, ensemble members are typically pre-trained by different research or application  
558 groups (Bodnar et al., 2025; Nearing et al., 2024; Song et al., 2025a), enabling direct reuse of  
559 these well-trained models and significantly improving computational efficiency.

560 For this work, we did not create a  $\delta$ HBV<sup>multi</sup> model (in the same vein as LSTM<sup>multi</sup>) using  
561 all forcings as an input to a single model, since a similar experiment has already been conducted  
562 by Sawadekar et al. (2025). We also did not examine “seed” combinations of a  $\delta$ HBV<sup>multi</sup> as  
563 we believed they would not result in a significant performance boost (unlike that seen with  
564 LSTM<sup>multi</sup>), because LSTM has high variability and low bias, while  $\delta$ HBV has lower variance  
565 and potentially higher bias. As a result, random seeds would likely not create large enough  
566 perturbations for  $\delta$ HBV and wouldn’t bring the benefits seen with  $LSTM_{seed}^{multi}$ . To achieve an  
567 equivalent perturbation level for  $\delta$ HBV, it may be necessary to incorporate multiple distinct  
568 hydrological models, such as SAC-SMA, PRMS, and GR4J, similar to the approach  
569 implemented in the Framework for Understanding Structural Errors (FUSE) ([Clark et al.,  
570 2008](#))[\(Clark et al., 2008\)](#). Work is ongoing to create a combination of a series of differentiable  
571 process-based models, which is expected to produce a further improved ensemble with great  
572 interpretability. Given the success of cross-model-type ensembles shown in this work, we also  
573 encourage further exploration of ensemble simulations involving models with other distinct  
574 mechanisms.

575

#### 576 4. Summary and conclusions

577 This study comprehensively analyzes ensemble combinations of two advanced model

578 types (LSTM and  $\delta$ HBV), each with distinct mechanisms, for streamflow simulation across  
579 531 basins in the US. Three meteorological forcing datasets (Daymet, NLDAS, and Maurer)  
580 are employed to fully capture the characteristics of the two models. Their applications are also  
581 tested in two distinct ways: (1) by feeding all diverse forcing datasets simultaneously into a  
582 single LSTM model, and (2) by ensembling the outputs of multiple LSTM models, each trained  
583 separately using a single forcing dataset. The performance of ensemble simulations was  
584 evaluated under three distinct testing scenarios (temporal, PUB, and PUR tests), surpassing the  
585 previous highest performances. Our findings enhance the understanding of how to effectively  
586 utilize diverse model types and multi-source datasets to improve streamflow simulations. The  
587 principal conclusions are:

588 (1) Cross-model-type ensembles (LSTM+ $\delta$ HBV) consistently outperformed single-  
589 model approaches across all test scenarios, setting new performance benchmarks on  
590 the CAMELS dataset. These ensembles demonstrated the complementarity of data-  
591 driven (LSTM) and physics-informed ( $\delta$ HBV) approaches in capturing diverse  
592 hydrological behaviors.

593 (2) Ensembling models trained on different forcing datasets proved more effective than  
594 using multiple forcing datasets as simultaneous inputs to a single model. This suggests  
595 that separate training allows each model to capture unique features contained in each  
596 forcing dataset, which can then be effectively leveraged in the ensemble.

597 (3)  $\delta$ HBV provided significant benefits to ensemble simulations on spatial generalization.  
598 Ensembling LSTM with  $\delta$ HBV showed increasing benefits as generalization  
599 challenges increased, from temporal to spatial interpolation (PUB) to spatial  
600 extrapolation (PUR) tests. This underscores the value of physics-informed constraints  
601 in improving model transferability to ungauged basins and regions.

602 (4) While ensemble methods significantly improved overall performance, they did not

603       fully mitigate consistent deficiencies in certain challenging areas (e.g., regions with  
604       high dam density or heterogeneous hydrogeological conditions). This indicates areas  
605       for future model development.

606       These findings have important implications for hydrological modeling and water  
607       resources management. The improved accuracy and spatial generalization of our ensemble  
608       approach can enhance streamflow predictions, benefiting water resources planning and  
609       management, particularly in data-scarce regions. Our results also suggest that future  
610       hydrological model development should focus on combining data-driven and physics-based  
611       approaches to improve model generalizability across diverse conditions. The superior  
612       performance of ensembling models with different forcing datasets over using merged forcings  
613       as a single input highlights the risk of indiscriminately feeding all available data into one data-  
614       driven model. While computational demands certainly require consideration, the potential  
615       improvements in prediction accuracy offer significant value for both research and operational  
616       applications. Future work should focus on refining these ensemble techniques, addressing  
617       model limitations in challenging regions, and exploring ensemble implementation in  
618       operational settings.

619 **Appendix A: Detailed processes of HBV employed in this study.**

620 The Hydrologiska Byråns Vattenbalansavdelning (HBV) model (Aghakouchak and Habib,  
 621 2010; Beck et al., 2020; Bergström, 1976, 1992) is a simple but effective bucket type  
 622 hydrologic model that simulates hydrologic variables including snow water equivalent, soil  
 623 water, groundwater storage, evapotranspiration, quick flow, baseflow, and total streamflow. In  
 624 the following texts, we describe these processes in detail by equations, in which uppercase  
 625 letters indicate state variables, and lowercase letters indicate model parameters. In general, the  
 626 water balance is developed based on Equation (S1).

627 The Hydrologiska Byråns Vattenbalansavdelning (HBV) model (Aghakouchak and Habib,  
 628 2010; Beck et al., 2020; Bergström, 1976, 1992) is a simple yet effective bucket-type  
 629 hydrologic model that simulates hydrologic components including snow water equivalent, soil  
 630 moisture, groundwater storage, evapotranspiration, quick flow, baseflow, and total streamflow.

631 In the following, we describe these processes in detail with their corresponding equations.  
 632 Uppercase letters denote state variables, while lowercase letters denote parameters. The overall  
 633 water balance is expressed as Equation (S1).

$$EP - AE - Q_t = SN + SM + UR + LRSUZ + SLZ + LAKE \quad (S1)$$

634 where  $EP$  is effective precipitation,  $AE$  is the actual evapotranspiration,  $Q_t$  is the total  
 635 simulated runoff,  $SN$  is snow storage,  $SM$  is soil water storage,  $UR$  is SUZ and  $SLZ$  are  
 636 the upper reservoir water level,  $LR$  is the and lower reservoir water level groundwater storages,  
 637 respectively, and  $LAKE$  is the represents lake level storage (omitted in this study).

638 First, effective precipitation ( $EP$ ) is separated into liquid rain ( $RN$ ) and solid snow ( $SN$ )  
 639 components based on the air temperature ( $T$ ) relative to the threshold temperature ( $tt$ ):

$$RN = EP \text{ if } T \geq tt \quad (S2)$$

$$SN = EP \text{ if } T < tt \quad (S3)$$

640 Snow ( $SN$ ) accumulates in the snowpack ( $SNP$ ), while the snowmelt ( $SNM$ ) happens when  $T \geq$   
 641  $tt$ , which is calculated using based on a temperature-dependent melt rate factor ( $cfm$ ) and the  
 642 temperature difference ( $T - tt$ ). The computed snowmelt ( $SNM$ ) is limited to constrained by the  
 643 available snowpack ( $SNP$ ), and any excess melt contributes to meltwater ( $MW$ ) as.

$$SNP = SNP + SN \quad (S4)$$

$$SNM = \begin{cases} SNP & cfm \cdot (T - tt) \geq SNP \\ cfm \cdot (T - tt) & T \geq tt, cfm \cdot (T - tt) < SNP \\ 0 & T < tt \end{cases} \quad (S5)$$

$$MW = MW + SNM \quad (S6)$$

$$\begin{aligned} SNP &= SNP - SNM \cdot SNM \\ &= \min[\max(cfr \cdot (T - tt), 0), SNP] \end{aligned} \quad (\text{S7S4})$$

644 Some of this The snowmelt (SNM) contributes to meltwater (MW) refreezes based on a  
 645 refreezing parameter (cfr) and the temperature difference from the threshold, returning to the  
 646 while the snowpack (SNP). The amount of refrozen water) is labeled updated as RFZ:

$$\begin{aligned} MW &= MW + SNM \cdot RFZ \\ &= \begin{cases} MW & \text{if } cfr \cdot cfm \cdot (tt - T) \geq MW \\ cfr \cdot cfm \cdot (tt - T) & \text{if } T < tt, cfr \cdot cfm \cdot (tt - T) < MW \\ 0 & \text{if } T \geq tt \end{cases} \quad (\text{S8S5}) \\ SNP &= SNP + RFZ \cdot SNM \quad (\text{S9S6}) \\ MW &= MW - RFZ \quad (\text{S10}) \end{aligned}$$

647 The remaining meltwater (MW) that exceeds the snowpack's holding capacity (cwh) contributes  
 648 to soil infiltration (IF), and the rest remains in the meltwater (MW) storage as  
 649 A portion of the meltwater (MW) may refreeze when  $T < tt$ , controlled by the refreezing  
 650 parameter (cfr):

$$\begin{aligned} IF &= \begin{cases} MW - cwh \cdot SNP & \text{if } MW - cwh \cdot SNP \geq 0 \\ 0 & \text{if } MW - cwh \cdot SNP < 0 \end{cases} \cdot RFZ \\ &= \min[\max(cfr \cdot cfm \cdot (tt - T), 0), MW] \end{aligned} \quad (\text{S11S7})$$

$$\begin{aligned} SNP &= SNP + RFZ \quad (\text{S8}) \\ MW &= MW - IF \cdot Z \quad (\text{S12S9}) \end{aligned}$$

651 The fraction of soil moisture relative to the field capacity (fc) determines the soil wetness,  
 652 which modulates the amount of water recharged into the soil (SP). Then soil moisture (SM) is  
 653 updated based on the infiltration of meltwater (IF), rain (RN), and the amount of recharged  
 654 water (SP) as

655 The remaining meltwater (MW) exceeding the snowpack's liquid water holding capacity (cwh ·  
 656 SNP) infiltrates into the soil (IF), with the remainder retained in MW:

$$\begin{aligned} IF &= \max(MW - cwh \cdot SNP, 0) \cdot SP = \left(\frac{SM}{fc}\right)^\beta \cdot (IF + RN) \quad (\text{S130}) \\ SM &= SM + MW = MW - IF + RN - SP \quad (\text{S141}) \end{aligned}$$

657 The excess water, above fraction of soil moisture (SM) relative to the field capacity ( $\frac{IF}{fc}$ ), is  
 658 calculated and subsequently removed from  $\frac{fc}{fc}$ , raised to the soil moisture storage as power index  
 659  $\beta$ , modulates shallow seepage (SP) according to the available water ( $IF + RN$ ):

$$SP = \left(\frac{SM}{fc}\right)^\beta \cdot \frac{IF}{fc} = \begin{cases} \frac{SM - fc}{fc} & \text{if } SM \geq fc \\ 0 & \text{if } SM < fc \end{cases} \cdot (IF + RN) \quad (\text{S152})$$

$$SM = SM - IF_{dir} + IF + RN - SP \quad (S163)$$

660 Actual evapotranspiration ( $AE$ ) is determined by an evaporation factor (PEC), which depends  
 661 on the soil moisture, a shape parameter ( $\lambda$ ), a parameter ( $lp$ ), and field capacity ( $fc$ ) for  
 662 evapotranspiration. This factor limits the actual evapotranspiration ( $AE$ ) to both the potential  
 663 evapotranspiration ( $PE$ ) and the available soil moisture.

664 Excess soil water above the field capacity contributes to direct infiltration ( $IF_{dir}$ ):

$$PEC = \begin{cases} \left( \frac{SM}{lp \cdot fc} \right)^\lambda & \text{if } 0 \leq \left( \frac{SM}{lp \cdot fc} \right)^\lambda \leq 1 \\ 0 & \text{if } S \left( \frac{SM}{lp \cdot fc} \right)^\lambda < 0 \\ 1 & \text{if } S \left( \frac{SM}{lp \cdot fc} \right)^\lambda \geq 1 \end{cases} \quad (S174)$$

$$= \max(SM - fc, 0)$$

$$AE = \begin{cases} PE \cdot PEC & \text{if } SM \geq PE \cdot PEC \\ SM & \text{if } SM < PE \cdot PEC \end{cases} \quad (S18)$$

$$SM = SM - AE \cdot IF_{dir} \quad (S195)$$

665 Capillary rise ( $CP$ ) from the lower soil zone ( $SLZ$ ) is governed by a parameter ( $c$ ), which  
 666 determines the amount of water moving upward based on the soil moisture content. This  
 667 capillary flow replenishes the soil moisture, while groundwater interactions occur through  
 668 recharge processes in the upper ( $SUZ$ ) and lower ( $SLZ$ ) groundwater zones.

669 Actual evapotranspiration ( $AE$ ) is estimated as the product of potential evapotranspiration ( $PE$ )  
 670 and an evapotranspiration coefficient ( $PEC$ ). The  $PEC$  depends on soil moisture storage ( $SM$ ),  
 671 field capacity ( $fc$ ), a shape parameter ( $\lambda$ ), and a threshold parameter ( $lp$ ).

$$CP = \begin{cases} SLZ & \text{if } SLZ < c \cdot SLZ \cdot \left( 1 - \frac{SM}{fc} \right) \\ c \cdot SLZ \cdot \left( 1 - \frac{SM}{fc} \right) & \text{if } SLZ \geq c \cdot SLZ \cdot \left( 1 - \frac{SM}{fc} \right) \end{cases} PEC$$

$$= \min \left[ 1, \max \left( 0, \left( \frac{SM}{lp \cdot fc} \right)^\lambda \right) \right] \quad (S20S16)$$

$$AE = \min(PE \cdot PEC, SM) \quad SM = SM + CP \quad (S217)$$

$$SLZ = \begin{cases} SLZ - CP & \text{if } SLZ \geq CP \\ 0 & \text{if } SLZ < CP \end{cases} \quad SM = SM - AE \quad (S22S18)$$

672 Excess recharge ( $SP$  and  $IF_{dir}$ ) from the soil enters the upper zone, where it either percolates  
 673 to the lower zone ( $PERC$ ) based on a constant rate ( $pre$ ) or contributes to direct runoff ( $Q_u$ )  
 674 when it exceeds the upper zone threshold ( $uzl$ ). The generated flow is modeled using

675 parameters ( $k_0, k_1, k_2$ ) governing flow from the upper and lower zones. Each of these flows  
 676 contributes to runoff ( $Q_0$ ). Capillary rise ( $CP$ ) from the lower zone ( $SLZ$ ) replenishes  $SM$ ,  
 677 controlled by a coefficient ( $c$ ) and constrained by the soil moisture deficit:  
 678  $, Q_1, Q_2$ , and their respective contributions to streamflow ( $Q_t$ ) are modeled over time.

$$CP = \min \left[ c \cdot SLZ \cdot \left( 1 - \frac{SM}{fc} \right), SLZ \right] SUZ = SUZ + SP + IF_{dir} \quad (S23S19)$$

$$SM = SM + CP \cdot PERC = \begin{cases} pre & \text{if } SUZ \geq pre \\ SUZ & \text{if } SUZ < pre \end{cases} \quad (S240)$$

$$SUZ = SUZ - PERC \quad (S25)$$

$$Q_0 = \begin{cases} k_0 \cdot (SUZ - uzl) & \text{if } SUZ \geq uzl \\ 0 & \text{if } SUZ < uzl \end{cases} \quad (S26)$$

$$SUZ = SUZ - Q_0 \quad (S27)$$

$$Q_1 = SUZ \cdot k_1 \quad (S28)$$

$$SUZ = SUZ - Q_1 \quad (S29)$$

$$SLZ = SLZ + PERC \quad (S30)$$

$$Q_2 = SLZ \cdot k_2 \quad (S31)$$

$$SLZ = SLZ - Q_2 \cdot CP \quad (S32)$$

$$Q_t = Q_0 + Q_1 + Q_2 \quad (S33)$$

679 Recharge from the soil, consisting of shallow seepage ( $SP$ ) and direct infiltration ( $IF_{dir}$ ), enters  
 680 the upper groundwater zone ( $SUZ$ ). Water in the upper zone either percolates to the lower  
 681 groundwater zone ( $SLZ$ ) at a constant percolation rate ( $prc$ ) or contributes to direct runoff ( $Q_0$ )  
 682 when the upper zone ( $SUZ$ ) exceeds a threshold ( $uzl$ ). Flow from the upper and lower zones is  
 683 computed using linear reservoir formulations, with parameters  $k_0, k_1, k_2$  controlling the  
 684 respective runoff components  $Q_0, Q_1, Q_2$ . The total simulated streamflow ( $Q_t$ ) is then  
 685 computed as the sum of these components.

686  
 687 Finally, a routing module (Feng et al., 2022) is used to process  $Q_t$  to produce the final  
 688 streamflow output ( $Q_t^*$ ). This module with two parameters ( $\theta_{eff}, \theta_{fit}$ ) assumes a gamma function  
 689 for the unit hydrograph and convolves the unit hydrograph with the runoff as,

$$SUZ = SUZ + SP + IF_{dir} Q_t^* = \int_0^{t_{max}} \xi(s; \theta_{eff}, \theta_{fit}) \cdot Q(t-s) ds \quad (S34S22)$$

$$\xi(s: \theta_\alpha, \theta_\tau) = \frac{1}{\Gamma(\theta_\alpha)\theta_\tau^{\theta_\alpha}} t^{\theta_\alpha-1} e^{-\frac{t}{\theta_\tau}} PERC = \min(prc, SUZ) \quad (\underline{S23})$$

$$SUZ = SUZ - PERC \quad (\underline{S24})$$

$$Q_0 = \max[k_0 \cdot (SUZ - uzl), 0] \quad (\underline{S25})$$

$$SUZ = SUZ - Q_0 \quad (\underline{S26})$$

$$Q_1 = SUZ \cdot k_1 \quad (\underline{S27})$$

$$SUZ = SUZ - Q_1 \quad (\underline{S28})$$

$$SLZ = SLZ + PERC \quad (\underline{S29})$$

$$Q_2 = SLZ \cdot k_2 \quad (\underline{S30})$$

$$SLZ = SLZ - Q_2 \quad (\underline{S31})$$

$$Q_t = Q_0 + Q_1 + Q_2 \quad (\underline{S32})$$

691

692 Finally, a routing module (Feng et al., 2022) is used to process  $Q_t$  to produce the final  
 693 streamflow output ( $Q_t^*$ ). This module with two parameters ( $\theta_\alpha, \theta_\tau$ ) assumes a gamma function  
 694 for the unit hydrograph and convolves the unit hydrograph with the runoff as,

695

$$Q_t^* = \int_0^{t_{max}} \xi(s: \theta_\alpha, \theta_\tau) \cdot Q(t-s) ds \quad (\underline{S33})$$

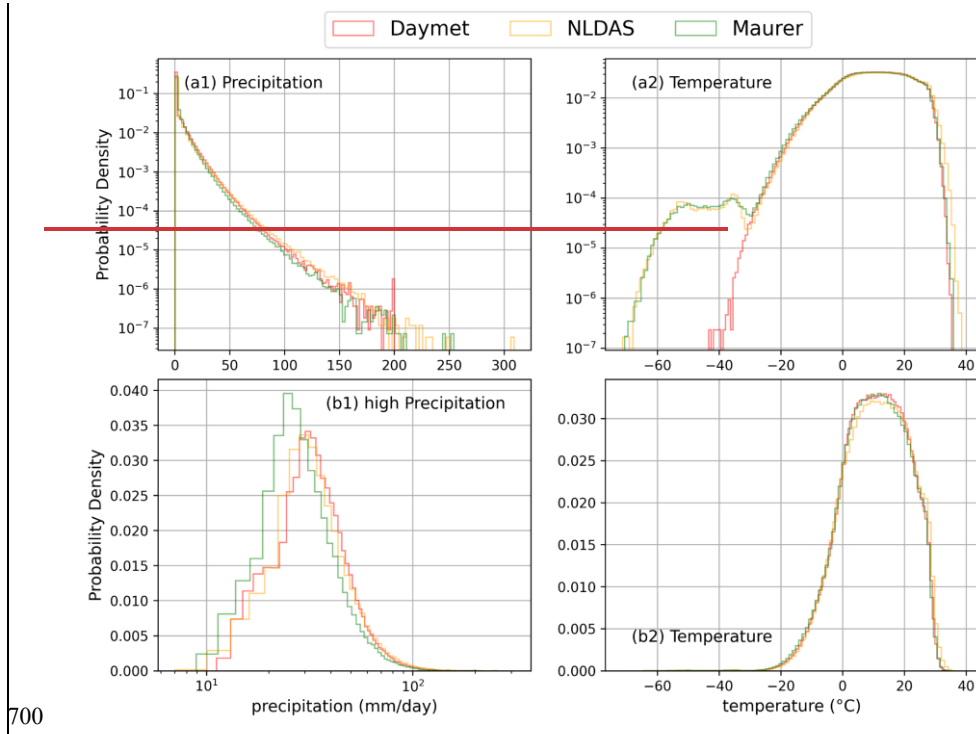
$$\xi(s: \theta_\alpha, \theta_\tau) = \frac{1}{\Gamma(\theta_\alpha)\theta_\tau^{\theta_\alpha}} t^{\theta_\alpha-1} e^{-\frac{t}{\theta_\tau}} \quad (\underline{S34})$$

696

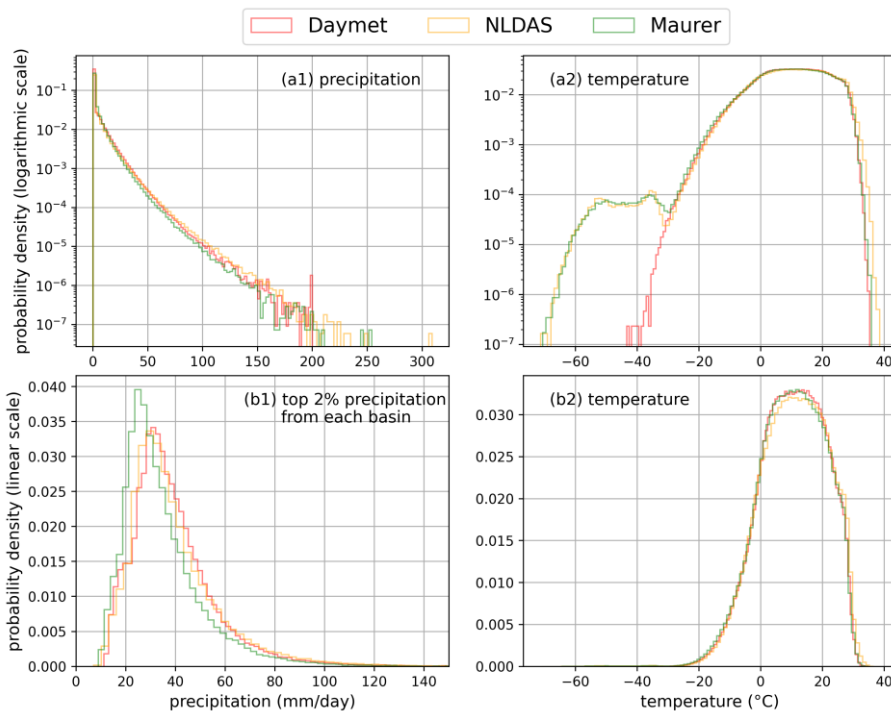
697

698

699 **Appendix B: Illustrated differences among the three meteorological forcing datasets**



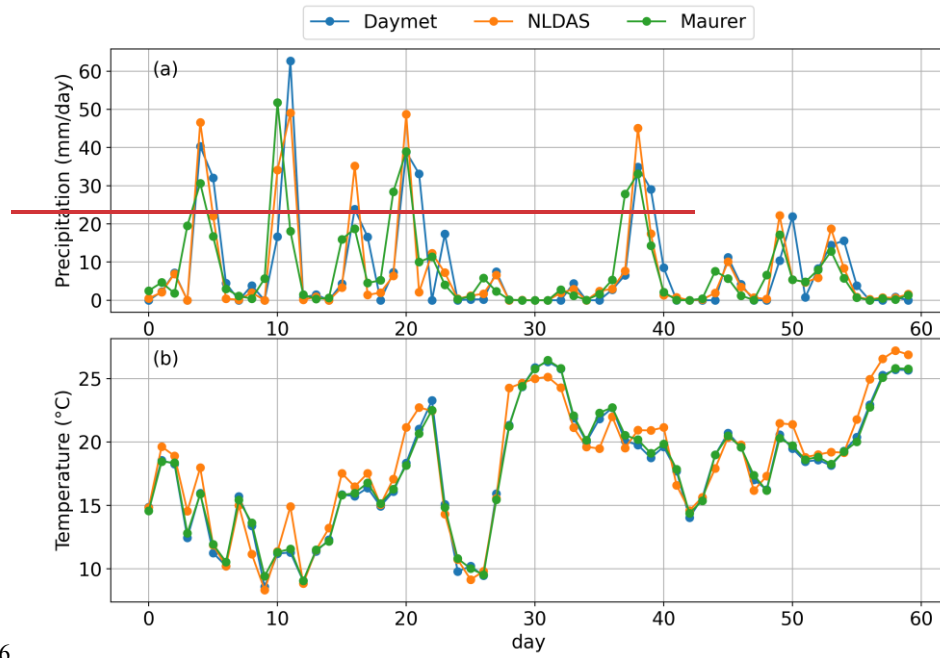
700



701  
702  
703  
704  
705

Figure B1. Probability density distributions ([top panel in logarithmic scale](#), [bottom panel in linear scale](#)) of precipitation and temperature across three meteorological forcing datasets.

706



707

708 Figure B2. Illustrated Example of temporal variations ~~of~~<sup>in</sup> precipitation and temperature ~~in~~

709 ~~at for one~~ basin across three meteorological forcing datasets.  
710

711 **Appendix C: Details of model inputs, ensemble frameworks, and evaluations**

712 *Table C1. Full names for the abbreviations of dynamic data (all but streamflow are “forcings”)*  
 713 *and static basin attributes used as model inputs and outputs. All variables and their values are*  
 714 *provided in the CAMELS dataset (Addor et al., 2017) except for the NLDAS and Maurer daily*  
 715 *temperature extrema, which are from Kratzert et al. (2021). Potential evapotranspiration and*  
 716 *normalized streamflow were calculated in this work, using CAMELS data. The number in*  
 717 *parentheses specifies model usage: 1 denotes use in the LSTM model, and 2*  
 718 *denotes use in the δHBV model.*

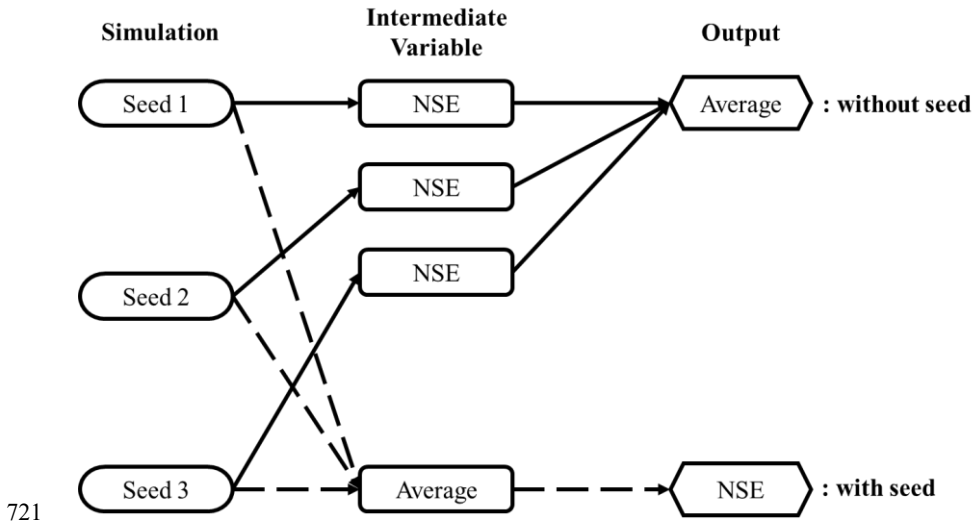
Type	Abbreviation	Full name	Unit
<b>Dynamic data</b>	prec (1,2)	Precipitation	mm/day
	pet (2)	Potential evapotranspiration (calculated in this work using the Hargreaves equation and CAMELS data)	mm/day
	tmean (2)	Mean air temperature	°C
	tmax (1)	Maximum air temperature	°C
	tmin (1)	Minimum air temperature	°C
	srad (1)	Shortwave radiation	W/m <sup>2</sup>
	vp (1)	Water vapor pressure	pa
	q_vol	Volumetric streamflow	ft <sup>3</sup> /s
	q (1,2)	Streamflow normalized by basin area (q_vol / area_gages2)	mm/day
<b>Static basin attributes</b>	p_mean (1,2)	Mean daily precipitation	mm/day
	pet_mean (1,2)	Mean daily potential evapotranspiration	mm/day
	p_seasonality (2)	Seasonality and timing of precipitation	-
	frac_snow (1,2)	Fraction of precipitation falling as snow	-
	aridity (1,2)	Rate of mean values of potential evapotranspiration and precipitation	-
	high_prec_freq (1,2)	Frequency of high precipitation days	days/year
	high_prec_dur (1,2)	Average duration of high precipitation events	days
	low_prec_freq (1,2)	Frequency of dry days	days/year
	low_prec_dur (1,2)	Average duration of dry periods	days

elev_mean (1,2)	Catchment mean elevation	m
slope_mean (1,2)	Catchment mean slope	m/km
area_gages2 (1,2)	Catchment area (GAGES-II estimate)	km <sup>2</sup>
frac_forest (1,2)	Fraction of catchment area having land cover identified as forest	-
lai_max (1,2)	Maximum monthly mean of the leaf area index	-
lai_diff (1,2)	Difference between the maximum and minimum monthly mean of the leaf area index	-
gvf_max (1,2)	Maximum monthly mean of the green vegetation	-
gvf_diff (1,2)	Difference between the maximum and minimum monthly mean of the green vegetation fraction	-
dom_land_cover_frac (2)	Fraction of the catchment area associated with the dominant land cover	-
dom_land_cover (2)	Dominant land cover type	-
root_depth_50 (2)	Root depth at 50 <sup>th</sup> percentile, extracted from a root depth distribution based on the International Geosphere-Biosphere Programme (IGBP) land cover	m
soil_depth_pelletier (1,2)	Depth to bedrock	m
soil_depth_statsgso (1,2)	Soil depth	m
soil_porosity (1,2)	Volumetric soil porosity	-
soil_conductivity (1,2)	Saturated hydraulic conductivity	cm/hr
max_water_content (1,2)	Maximum water content	m
sand_frac (1,2)	Fraction of soil which is sand	-

	silt_frac (1,2)	Fraction of soil which is silt	-
	clay_frac (1,2)	Fraction of soil which is clay	-
	geol_class_1st (2)	Most common geologic class in the catchment basin	-
	geol_class_1st_frac (2)	Fraction of the catchment area associated with its most common geologic class	-
	geol_class_2nd (2)	Second most common geologic class in the catchment basin	-
	geol_class_2nd_frac (2)	Fraction of the catchment area associated with its 2nd most common geologic class	-
	carbonate_rocks_frac (1,2)	Fraction of the catchment area as carbonate sedimentary rocks	-
	geol_porosity (2)	Subsurface porosity	-
	geol_permeability (1,2)	Subsurface permeability	m <sup>2</sup>

719

720



722 *Figure C1. Ensemble frameworks to generate metrics for ensembles named without (solid arrows) and with (dashed arrows) "seed" as a subscript.*

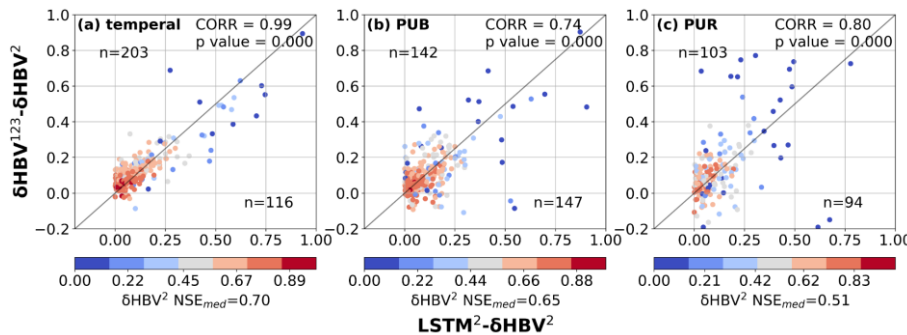
724 Table C2. *Evaluation* Loss function and evaluation metrics.

Statistic	Equation*	Range	Optimal Value
Loss	$\frac{1}{n} \sum_{i=1}^n \frac{(O_i - S_i)^2}{(\sigma_o + \epsilon)^2}$	0.0 to $\infty$	0.0
NSE	$1 - \frac{\sum_{i=1}^n (O_i - S_i)^2}{\sum_{i=1}^n (O_i - \mu_o)^2}$	$-\infty$ to 1.0	1.0
KGE	$1 - \sqrt{(r - 1)^2 + (\beta - 1)^2 + (\gamma - 1)^2},$ $\beta = \frac{\mu_S}{\mu_O}, \gamma = \frac{CV_S}{CV_O} = \frac{\sigma_S/\mu_S}{\sigma_O/\mu_O}$	$-\infty$ to 1.0	1.0
PBIAS	$\frac{\sum_{i=1}^n (O_i - S_i)}{\sum_{i=1}^n O_i} \times 100$	$-\infty$ to $\infty$	0.0
RMSE	$\sqrt{\frac{1}{n} \sum_{i=1}^n (O_i - S_i)^2}$	0.0 to $\infty$	0.0
spread	$\sqrt{\frac{1}{n} \frac{1}{e} \sum_{i=1}^n \sum_{j=1}^e (S_{i,j} - \mu_{S,i})^2}$	0.0 to $\infty$	None

725 \*  $S$  is the streamflow simulation;  $O$  is the corresponding observation;  $n$  is the number of total  
 726  $S$  or  $O$ ;  $\epsilon$  is a numerical stabilizer, with a default value of 0.1;  $e$  is the number of ensemble  
 727 members;  $r$  is the linear Pearson correlation between  $S$  and  $O$ ;  $\beta$  is the mean bias; and  $\gamma$  is the  
 728 variability bias. The mean and standard deviation of simulations are denoted as  $\mu_S$  and  $\sigma_S$ ,  
 729 respectively, and while  $\mu_0$  and  $\sigma_0$  are the mean and standard deviation denote those of the  
 730 observations.

731 **Appendix D: Additional details on model performance**

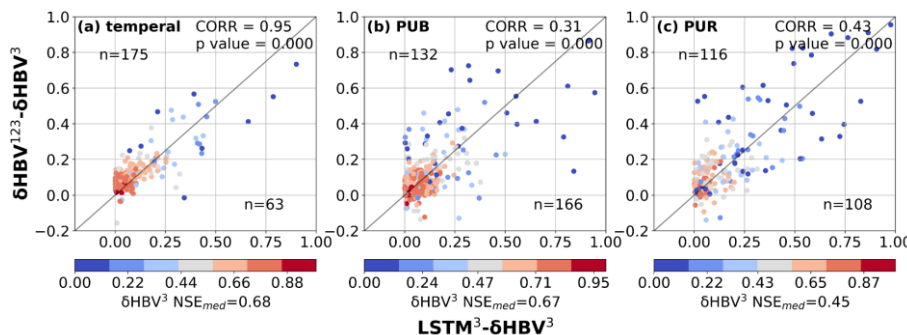
732



733

734 *Figure D1. Scatter plots comparing the performance differences between hydrological models*  
735 *for the basins where LSTM outperformed  $\delta$ HBV (the basins where  $\delta$ HBV outperformed are not*  
736 *shown in this plot). The x-axis represents the NSE differences between  $LSTM^2$  and  $\delta$ HBV<sup>2</sup>*  
737 *( $LSTM^2 - \delta$ HBV<sup>2</sup>), while the y-axis shows the NSE differences between  $\delta$ HBV<sup>123</sup> and  $\delta$ HBV<sup>2</sup>*  
738 *( $\delta$ HBV<sup>123</sup> -  $\delta$ HBV<sup>2</sup>). Points are color-coded according to the NSE values of  $\delta$ HBV<sup>2</sup>. The*  
739 *correlation coefficient (CORR) and p values between the x-axis values and the y-axis values,*  
740 *along with the median NSE value of  $\delta$ HBV<sup>2</sup> (NSE<sub>med</sub>) on these basins, are also noted.*

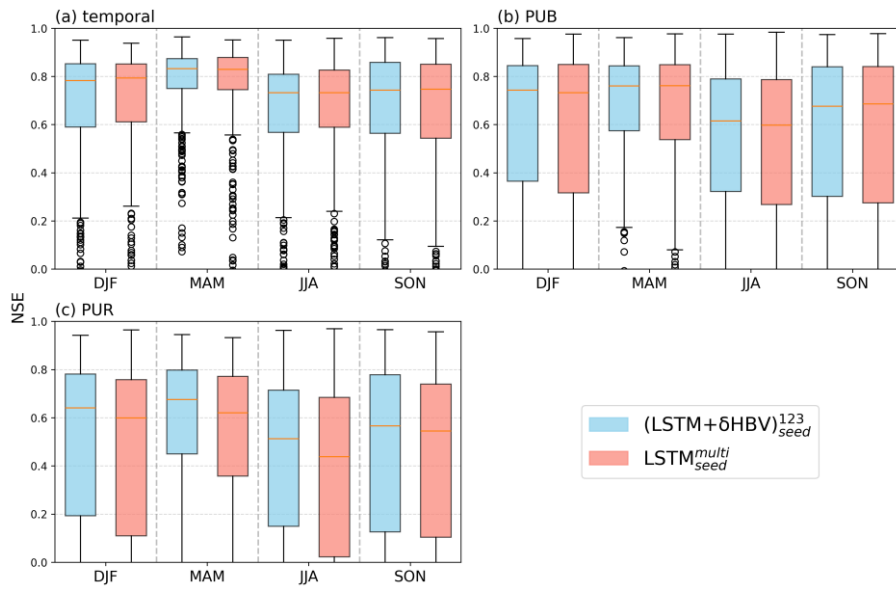
741



742

743 *Figure D2. Scatter plots comparing the performance differences between hydrological models*  
744 *for the basins where LSTM outperformed  $\delta$ HBV (the basins where  $\delta$ HBV outperformed are not*  
745 *shown in this plot). The x-axis represents the NSE differences between  $LSTM^3$  and  $\delta$ HBV<sup>3</sup>*  
746 *( $LSTM^3 - \delta$ HBV<sup>3</sup>), while the y-axis shows the NSE differences between  $\delta$ HBV<sup>123</sup> and  $\delta$ HBV<sup>3</sup>*  
747 *( $\delta$ HBV<sup>123</sup> -  $\delta$ HBV<sup>3</sup>). Points are color-coded according to the NSE values of  $\delta$ HBV<sup>3</sup>. The*  
748 *correlation coefficient (CORR) and p values between the x-axis values and the y-axis values,*  
749 *along with the median NSE value of  $\delta$ HBV<sup>3</sup> (NSE<sub>med</sub>) on these basins, are also noted.*

750

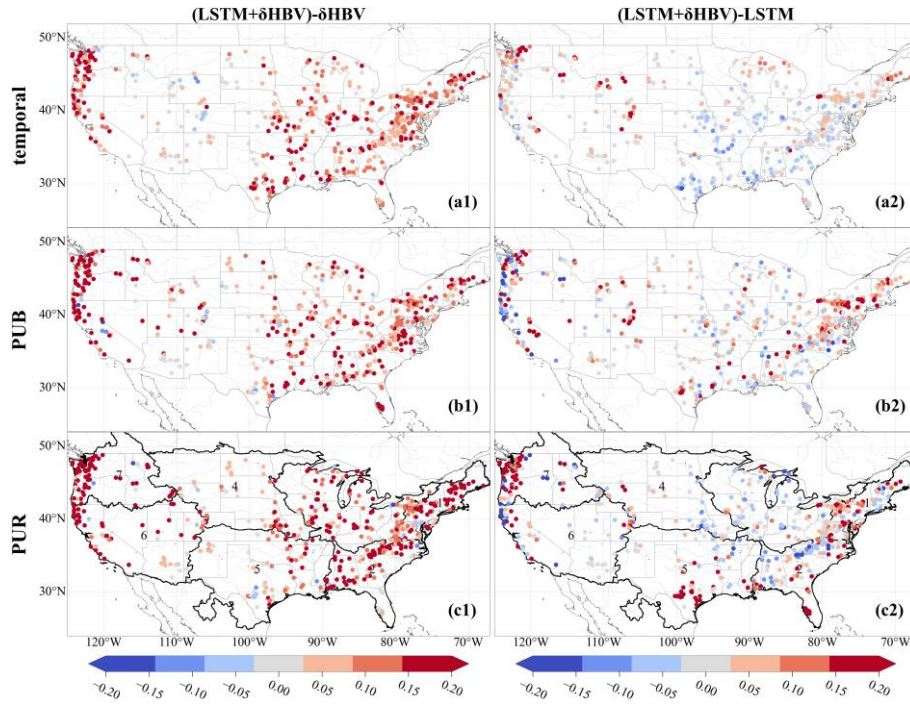


751

752 *Figure D3. Seasonal comparison of NSE values for  $(LSTM + \delta HBV)^{123}_{seed}$  (blue) and*  
753  *$LSTM_{seed}^{multi}$  (red) in (a) temporal, (b) PUB, and (c) PUR tests. Each box represents the*  
754 *distribution of NSE values across 531 basins for a given season (DJF: December–February,*  
755 *MAM: March–May, JJA: June–August, SON: September–November). Vertical dashed lines*  
756 *separate different seasons.  $(LSTM + \delta HBV)^{123}_{seed}$  performs better than  $LSTM_{seed}^{multi}$  in most*  
757 *cases, especially during MAM, likely due to differences in snowmelt representation.*

758

759



760  
761 *Figure D3-D4.* Spatial distributions of model spread values increase from  $\delta\text{HBV}$  and LSTM to  
762 the LSTM+ $\delta\text{HBV}$  ensemble across temporal, PUB, and PUR tests.

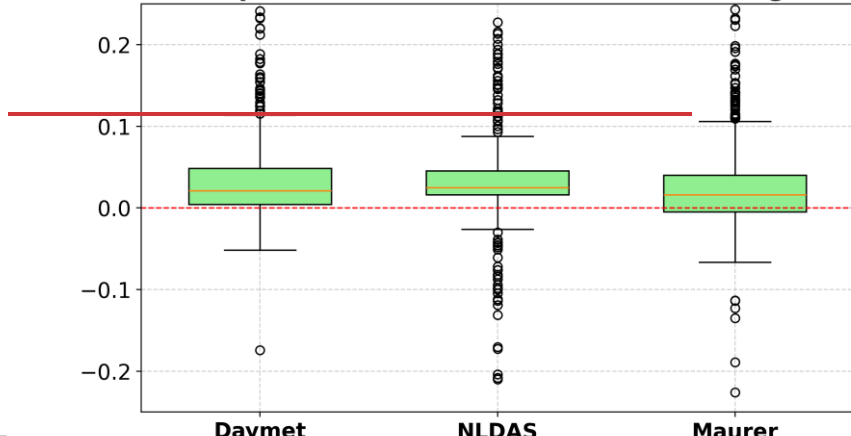
763

764

765

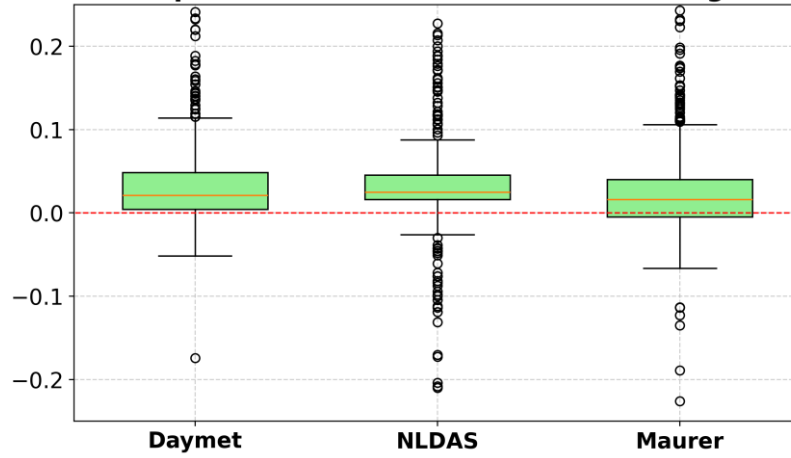
766

### Relative Temperature Differences: (Test – Training) / Training



767

### relative temperature differences: (test – training) / training



768

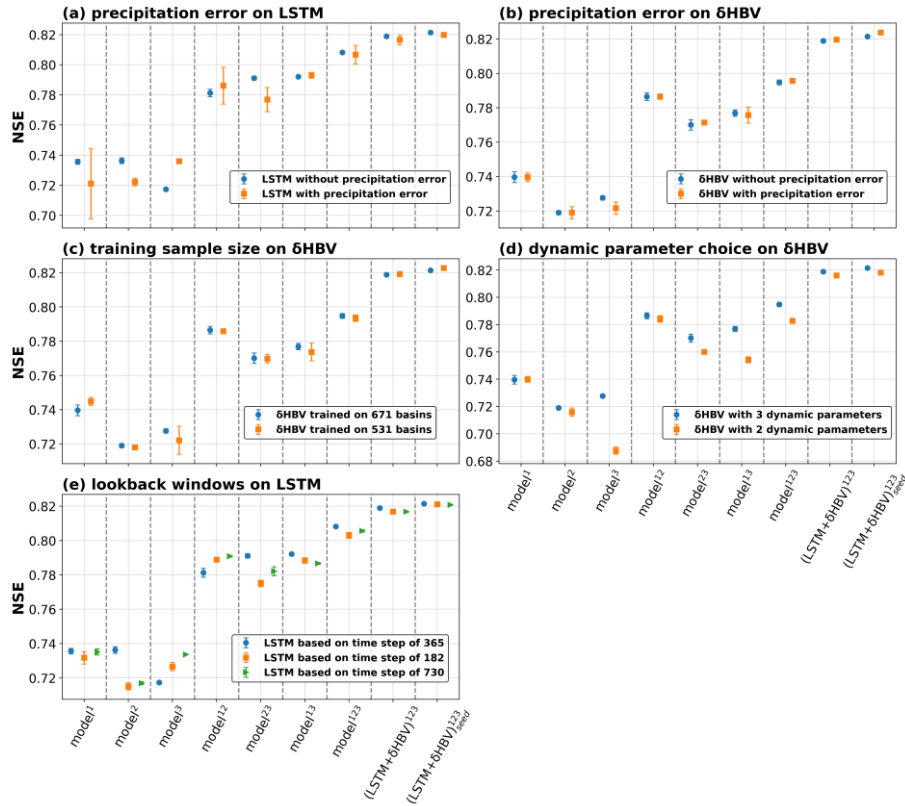
769 *Figure D4D5.* Boxplot of relative temperature differences between the test and training periods,  
770 calculated as  $(\text{Test} - \text{Training}) / \text{Training}$ . Each box represents the  
771 distribution of normalized temperature changes across basins for a specific meteorological  
772 forcing dataset: Daymet, NLDAS, and Maurer. Positive values indicate warming in the test  
773 period relative to the training period.

774

775

776

777



778  
779 Figure D5D6. Simulation performance (NSE) under the temporal test: (a) LSTM model with  
780 and without a 10% precipitation error (precipitation  $\times 1.1$ ); (b)  $\delta$ HBV model with and without  
781 a 10% precipitation error; (c)  $\delta$ HBV model trained on 671 versus 531 basins; (d)  $\delta$ HBV model  
782 with 3 versus 2 dynamic parameters; (e)  $\delta$ HBV model using time steps of 365, 182, and 730  
783 days. Individual and ensemble groups are distinguished along the x-axis. Ensemble benefits  
784 are indicated by the gap between columns of the same color within each panel—columns 1–7  
785 correspond to individual LSTM or  $\delta$ HBV groups, and the last two columns correspond to  
786 LSTM+ $\delta$ HBV ensembles.

787

788

789 *Table D1. Median NSE, KGE, RMSE, PBIAS, and RMSE values under low (lowRMSE), high*  
 790 *(highRMSE), and middle (midRMSE) flows based on 531 basins under the temporal test. The*  
 791 *values are the mean of three simulations run with different random seeds.*

Temporal	Number	Daymet	NLDAS	Maurer
LSTM	NSE	0.735639	0.736301	0.717337
	KGE	0.789375	0.782555	0.760575
	RMSE	1.21088	1.19847	1.27723
	PBIAS	4.04818	5.99486	1.58911
	lowRMSE	0.0596913	0.0602381	0.0545577
	highRMSE	2.70508	2.89684	2.97028
	midRMSE	0.196039	0.210022	0.219922
$\delta$ HBV	NSE	0.739688	0.71903	0.727669
	KGE	0.77033	0.730753	0.762022
	RMSE	1.18752	1.26239	1.23193
	PBIAS	5.07898	-0.14449	3.65263
	lowRMSE	0.060906	0.063581	0.063466
	highRMSE	2.68479	3.13011	2.6845
	midRMSE	0.226595	0.245242	0.230125
LSTM+ $\delta$ HBV	NSE	0.787545	0.794053	0.790903

KGE	0.794412	0.78383	0.786854
RMSE	1.0777	1.0716	1.07141
PBIAS	4.59065	3.33053	3.45501
lowRMSE	0.059955	0.059565	0.054838
highRMSE	2.70216	2.88511	2.69633
midRMSE	0.20394	0.214726	0.212514

792

793

794

795 *Table D1 (continued). Median NSE, KGE, RMSE, PBIAS, and RMSE values under low*  
 796 *(lowRMSE), high (highRMSE), and middle (midRMSE) flows based on 531 basins under the*  
 797 *temporal test. The values are the mean of three simulations run with different random seeds.*

Temporal	Number	Daymet+NLDAS	Daymet+Maurer	NLDAS+Maurer	All
LSTM	NSE	0.781275	0.791158	0.792144	0.808176
	KGE	0.800955	0.795026	0.794441	0.803476
	RMSE	1.09103	1.06374	1.06701	1.01395
	PBIAS	5.17159	3.34362	4.5305	4.48263
	lowRMSE	0.0636155	0.0582563	0.0566306	0.0613625
	highRMSE	2.70218	2.71366	2.78962	2.67803
	midRMSE	0.194849	0.199809	0.206653	0.197469
δHBV	NSE	0.786562	0.77012	0.776938	0.794796
	KGE	0.773732	0.778557	0.768854	0.77834
	RMSE	1.08362	1.12584	1.10875	1.06118
	PBIAS	1.91507	4.28194	2.03584	2.71021
	lowRMSE	0.061667	0.060679	0.062765	0.061539
	highRMSE	2.93961	2.7394	2.88758	2.84994
	midRMSE	0.230576	0.220743	0.230272	0.228375
LSTM+δHBV	NSE	0.811825	0.809964	0.811316	0.818907

KGE	0.797564	0.797635	0.78735	0.794936
RMSE	1.01938	1.01755	1.0314	1.00067
PBIAS	4.14594	4.23333	3.19652	3.88096
lowRMSE	0.0603	0.058022	0.057882	0.059221
highRMSE	2.75275	2.67122	2.81393	2.70606
midRMSE	0.207637	0.205965	0.213191	0.207905

798

799 Table D2. Median NSE, KGE, RMSE, PBIAS, and RMSE values under low (lowRMSE), high  
 800 (highRMSE), and middle (midRMSE) flows based on 531 basins under the PUB test. The values  
 801 are the mean of three simulations run with different random seeds.

PUB	Number	Daymet	NLDAS	Maurer
LSTM	NSE	0.702636	0.695496	0.694156
	KGE	0.693998	0.677438	0.6909
	RMSE	1.31714	1.3394	1.34233
	PBIAS	0.669018	0.283106	0.936582
	lowRMSE	0.087648	0.088393	0.086873
	highRMSE	4.2852	4.49292	4.16042
	midRMSE	0.354458	0.364921	0.368124
δHBV	NSE	0.706809	0.670636	0.682998
	KGE	0.703137	0.66566	0.686912
	RMSE	1.35541	1.41185	1.37942
	PBIAS	1.49234	-2.43395	0.291966
	lowRMSE	0.0798196	0.0808967	0.0846775
	highRMSE	4.21648	4.49582	4.18003
	midRMSE	0.335159	0.351271	0.356903
LSTM+δHBV	NSE	0.74227	0.723778	0.72202

KGE	0.715931	0.690154	0.707292
RMSE	1.24887	1.278	1.26697
PBIAS	1.27863	-0.599778	0.903464
lowRMSE	0.0816748	0.0795686	0.0825691
highRMSE	4.08432	4.23483	3.94929
midRMSE	0.327459	0.33851	0.347169

802  
803  
804

805 *Table D2 (continued). Median NSE, KGE, RMSE, PBIAS, and RMSE values under low*  
 806 *(lowRMSE), high (highRMSE), and middle (midRMSE) flows based on 531 basins under the*  
 807 *PUB test. The values are the mean of three simulations run with different random seeds.*

PUB	Number	Daymet+NLDAS	Daymet+Maurer	NLDAS+Maurer	All
LSTM	NSE	0.757853	0.749151	0.753136	0.768181
	KGE	0.713319	0.720099	0.716497	0.727143
	RMSE	1.18251	1.22254	1.19718	1.15026
	PBIAS	0.320396	0.931656	0.766216	0.970047
	lowRMSE	0.0875191	0.0864129	0.0835341	0.0874717
	highRMSE	4.1296	4.06602	4.17217	4.0061
	midRMSE	0.334683	0.349856	0.342819	0.333534
δHBV	NSE	0.748916	0.734052	0.733955	0.757749
	KGE	0.699768	0.714323	0.69436	0.714048
	RMSE	1.26852	1.27637	1.27244	1.23229
	PBIAS	0.0446112	1.212	-1.04135	0.201809
	lowRMSE	0.0808293	0.0792486	0.0814476	0.0808359
	highRMSE	4.19575	3.97788	4.21623	4.07419
	midRMSE	0.311826	0.33668	0.339257	0.318165
LSTM+δHBV	NSE	0.780625	0.764866	0.767761	0.785833

KGE	0.719781	0.725373	0.715982	0.723972
RMSE	1.14924	1.17659	1.16881	1.13591
PBIAS	0.186062	0.881644	0.405548	0.565489
lowRMSE	0.0805946	0.0814251	0.0817114	0.0826379
highRMSE	3.97373	3.86834	3.88	3.91692
midRMSE	0.313708	0.324777	0.324089	0.323671

808

809

810 *Table D3. Median NSE, KGE, RMSE, PBIAS, and RMSE values under low (lowRMSE), high*  
 811 *(highRMSE), and middle (midRMSE) flows based on 531 basins under the PUR test. The values*  
 812 *are the mean of three simulations run with different random seeds.*

PUR	Number	Daymet	NLDAS	Maurer
LSTM	NSE	0.578365	0.546217	0.56164
	KGE	0.557788	0.559986	0.567231
	RMSE	1.59111	1.63626	1.5833
	PBIAS	-0.575328	-2.77709	-0.623183
	lowRMSE	0.124837	0.118971	0.118695
	highRMSE	5.42346	5.38886	5.05212
	midRMSE	0.498133	0.498442	0.471744
δHBV	NSE	0.622278	0.592306	0.59161
	KGE	0.638818	0.601338	0.620877
	RMSE	1.57189	1.61191	1.63628
	PBIAS	1.27223	-1.60075	1.62709
	lowRMSE	0.10142	0.102975	0.101075
	highRMSE	5.07706	5.16093	4.99602
	midRMSE	0.447879	0.474516	0.439697
LSTM+δHBV	NSE	0.644398	0.618255	0.635444

KGE	0.627481	0.605237	0.615883
RMSE	1.46185	1.5153	1.48393
PBIAS	-0.269697	-0.719505	0.197859
lowRMSE	0.105146	0.100944	0.106272
highRMSE	4.95749	4.99478	4.78638
midRMSE	0.431456	0.4575	0.426126

813

814

815 *Table D3 (continued). Median NSE, KGE, RMSE, PBIAS, and RMSE values under low*  
 816 *(lowRMSE), high (highRMSE), and middle (midRMSE) flows based on 531 basins under the*  
 817 *PUR test. The values are the mean of three simulations run with different random seeds.*

PUR	Number	Daymet+NLDAS	Daymet+Maurer	NLDAS+Maurer	All
LSTM	NSE	0.634398	0.636369	0.626939	0.656228
	KGE	0.59844	0.600371	0.605007	0.612858
	RMSE	1.4434	1.43416	1.43009	1.38042
	PBIAS	-0.547128	-0.687947	-0.865748	-0.543918
	lowRMSE	0.118989	0.120228	0.115004	0.117728
	highRMSE	5.03277	5.02434	4.84415	4.74281
	midRMSE	0.462923	0.455257	0.453912	0.449598
δHBV	NSE	0.672839	0.644732	0.661231	0.684685
	KGE	0.653841	0.65646	0.6515	0.66205
	RMSE	1.43224	1.50803	1.48604	1.43376
	PBIAS	0.564363	1.55134	-0.156553	0.956961
	lowRMSE	0.0975783	0.0984076	0.100773	0.100807
	highRMSE	4.83843	4.81176	4.72529	4.71255
	midRMSE	0.447828	0.431252	0.433688	0.432018
LSTM+δHBV	NSE	0.685032	0.680872	0.679321	0.700814

KGE	0.638788	0.647826	0.646782	0.649999
RMSE	1.35303	1.3873	1.36795	1.3185
PBIAS	-0.0150729	0.406127	-0.135091	-0.0232668
lowRMSE	0.103284	0.101814	0.104528	0.102916
highRMSE	4.80178	4.72583	4.70024	4.70713
midRMSE	0.426819	0.411727	0.41573	0.41081

818

819

820 *Table D4. Median NSE, KGE, RMSE, PBIAS, and RMSE values under low (lowRMSE), high*  
 821 *(highRMSE), and middle (midRMSE) flows based on 531 basins under the temporal, PUB, and*  
 822 *PUR tests of  $LSTM^{multi}$ ,  $(LSTM + \delta HBV)^{123}$  +  $LSTM^{multi}$ , their “seed” version, and*  
 823  *$(LSTM + \delta HBV)^{123}_{seed}$ .*

Test	Metric	$LSTM^{multi}$	$(LSTM + \delta HBV)^{123}$ + $LSTM^{multi}$
Temporal	NSE	0.797448	0.82321
	KGE	0.811064	0.810248
	RMSE	1.05987	0.983168
	PBIAS	3.95241	4.08594
	lowRMSE	0.056221	0.05702
	highRMSE	2.7089	2.58881
	midRMSE	0.183526	0.192442
PUB	NSE	0.750605	0.782727
	KGE	0.71469	0.734731
	RMSE	1.20586	1.11509
	PBIAS	0.475674	0.706777
	lowRMSE	0.0861127	0.0836
	highRMSE	4.13615	3.83009
	midRMSE	0.347562	0.326814

PUR	NSE	0.623755	0.68923
	KGE	0.593757	0.633971
	RMSE	1.47379	1.31221
	PBIAS	-2.6737	-1.38119
	lowRMSE	0.112434	0.107646
	highRMSE	4.98202	4.59232
	midRMSE	0.501807	0.436811

824

825 *Table D4 (continued). Median NSE, KGE, RMSE, PBIAS, and RMSE values under low*  
 826 *(lowRMSE), high (highRMSE), and middle (midRMSE) flows based on 531 basins under the*  
 827 *temporal, PUB, and PUR tests of  $LSTM^{multi}$ ,  $(LSTM + \delta HBV)^{123}$  +  $LSTM^{multi}$ , their “seed”*  
 828 *version, and  $(LSTM + \delta HBV)^{123}_{seed}$ .*

Test	Metric	$(LSTM + \delta HBV)^{123}_{seed}$	$LSTM^{multi}_{seed}$	$(LSTM + \delta HBV)^{123}_{seed}$ + $LSTM^{multi}_{seed}$
Temporal	NSE	0.821444	0.81992	0.829385
	KGE	0.795317	0.82078	0.812581
	RMSE	0.99455	1.00908	0.967779
	PBIAS	3.99009	4.09469	4.08882
	lowRMSE	0.059782	0.057346	0.057015
	highRMSE	2.7279	2.62815	2.58384
	midRMSE	0.209943	0.183656	0.195557
PUB	NSE	0.793673	0.781175	0.790921
	KGE	0.726188	0.736191	0.739284
	RMSE	1.12957	1.13079	1.09176
	PBIAS	0.370674	1.13671	0.869057
	lowRMSE	0.083423	0.084038	0.085728
	highRMSE	3.89363	3.93473	3.79505
	midRMSE	0.323045	0.329772	0.325627

PUR	NSE	0.705154	0.665723	0.701504
	KGE	0.651538	0.614649	0.64373
	RMSE	1.30377	1.3727	1.2851
	PBIAS	-0.283645	-2.74069	-1.39149
	lowRMSE	0.100525	0.111229	0.108121
	highRMSE	4.74889	4.88127	4.58344
	midRMSE	0.406797	0.473783	0.432447

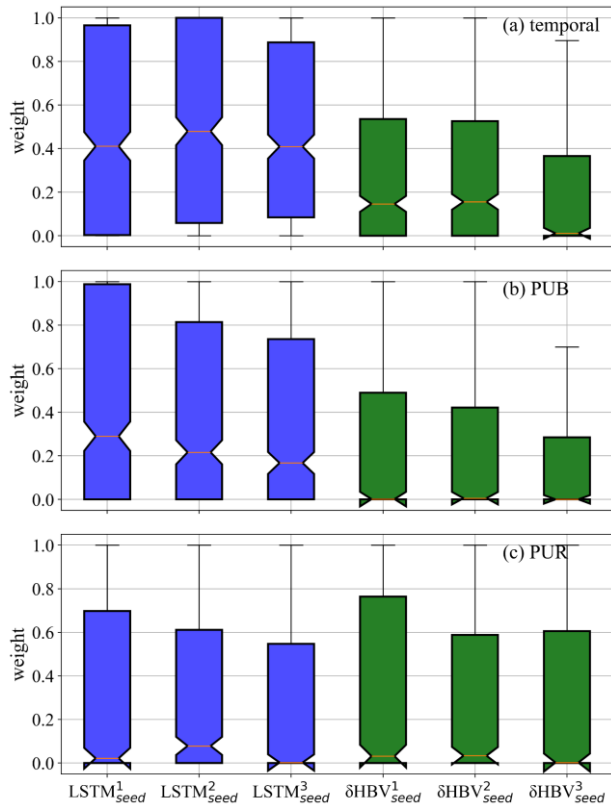
829

830 *Table D5. Median NSE values based on ten different random seeds during the temporal test.*  
 831 *Each number (1 through 10) represents metric values calculated for an individual simulation*  
 832 *based on only one random seed. “Seed” indicates metric values calculated by averages of these*  
 833 *ten simulations based on different random seeds, while “mean” denotes the average of metrics*  
 834 *from 1-10 individual simulations (visualized in Figure C1).*

Number	$LSTM^{multi}$	$(LSTM + \delta HBV)^{123}$	$(LSTM + \delta HBV)^{123} + LSTM^{multi}$
1	0.797742	0.818436	0.82315
2	0.795312	0.820188	0.823559
3	0.799291	0.818097	0.822922
4	0.796388	0.818251	0.821791
5	0.791192	0.818285	0.820132
6	0.795691	0.81966	0.823268
7	0.795912	0.821511	0.82352
8	0.796625	0.81831	0.825204
9	0.794062	0.804959	0.816497
10	0.796066	0.817122	0.82169
Seed	0.82425	0.822528	0.832197
Mean	0.795828	0.817482	0.822173

835

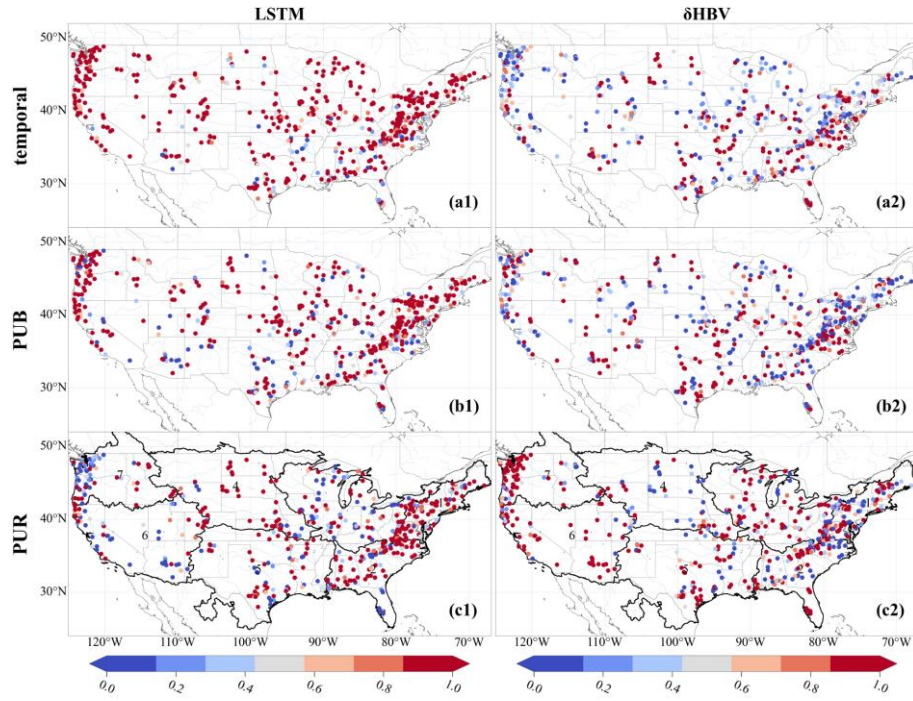
836 **Appendix E: Intuitive visualization of the relative contributions of ensemble members**  
837 **based on optimized weights**



838

839 *Figure E1. Weights of six components across 531 basins, estimated basin-by-basin using a*  
840 *genetic algorithm based on streamflow observations during the test periods. The weights are*  
841 *normalized by the maximum weight within each ensemble group. These weights are used*  
842 *exclusively for qualitatively analyzing the relative contributions of different ensemble members,*  
843 *with higher values indicating larger relative contributions.*

844

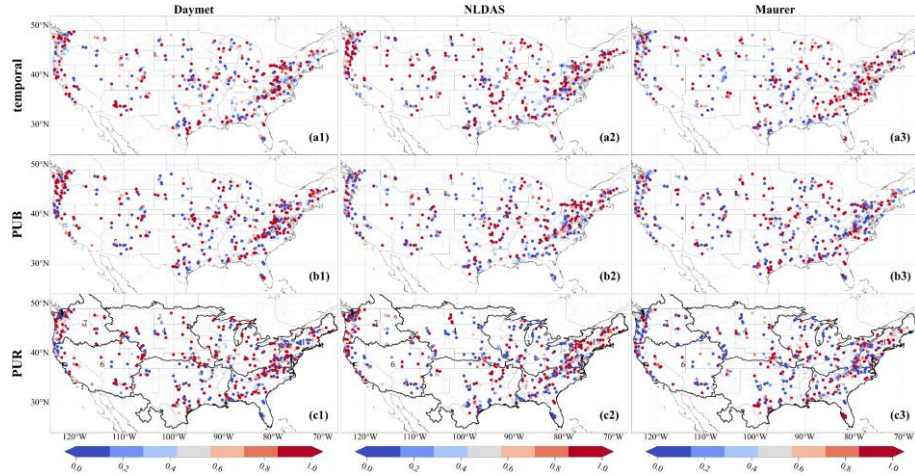


845

846 *Figure E2. Spatial distributions of weights of the LSTM and  $\delta$ HBV models, estimated by a*  
 847 *genetic algorithm based on streamflow observations during the test periods. The weights are*  
 848 *normalized by the maximum weight within each ensemble group. These weights are used*  
 849 *exclusively for qualitatively analyzing the relative contributions of different ensemble members,*  
 850 *with higher values indicating larger relative contributions.*

851

852



853

854 *Figure E3. Spatial distributions of weights of the Daymet, NLDAS, and Maurer meteorological*  
 855 *forcing datasets, estimated by a genetic algorithm based on streamflow observations during*  
 856 *the test periods. The weights are normalized by the maximum weight within each ensemble*  
 857 *group. These weights are used exclusively for qualitatively analyzing the relative contributions*  
 858 *of different ensemble members, with higher values indicating larger relative contributions.*

859

860

861

862 *Table E1. Comparisons of metric values between averaged ensemble simulations and*  
 863 *optimized weighted simulations, estimated using a genetic algorithm based on streamflow*  
 864 *observations during the test periods. The results highlight the potential for further*  
 865 *improvements in ensemble simulations.*

866

	Temporal	Averaged	Optimized weighted
Temporal	NSE	0.821444	0.844303212
	KGE	0.795317	0.829996445
	RMSE	0.99455	0.920954559
	PBIAS	3.99009	3.252278013
	lowRMSE	0.059782	0.057137161
	highRMSE	2.7279	2.451194907
	midRMSE	0.209943	0.183127162
PUB	NSE	0.793673	0.842396015
	KGE	0.726188	0.79571295
	RMSE	1.12957	0.987170488
	PBIAS	0.370674	1.023040859
	lowRMSE	0.0834234	0.079807878
	highRMSE	3.89363	3.030715903
	midRMSE	0.323045	0.285110115
PUR	NSE	0.705154	0.790796063
	KGE	0.651538	0.746396324
	RMSE	1.30377	1.13058149

PBIAS	-0.283645	0.273698787
lowRMSE	0.100525	0.093595304
highRMSE	4.74889	3.665495069
midRMSE	0.406797	0.351694421

867

868

869 **Code and data availability**

870 The source codes and datasets utilized in this study are publicly accessible through the  
871 following repositories: The  $\delta$ HBV modeling framework, including all computational scripts  
872 and documentation, is hosted on Zenodo (<https://doi.org/10.5281/zenodo.7091334>) (Feng et al.,  
873 2023a)(Feng et al., 2023a), with an updated version and comprehensive software release  
874 scheduled upon manuscript acceptance. The implementation of the LSTM architecture is  
875 accessible through Zenodo (<https://doi.org/10.5281/zenodo.6326394>) (Kratzert et al.,  
876 2022)(Kratzert et al., 2022). The CAMELS hydrometeorological dataset, which provides the  
877 foundational basin characteristics and time series data used in our analysis, can be obtained via  
878 <https://dx.doi.org/10.5065/D6MW2F4D> (Addor et al., 2017; Newman and Clark, 2014)(Addor  
879 et al., 2017; Newman and Clark, 2014). The streamflow simulations produced in this study will  
880 be made available on Zenodo upon acceptance of the manuscript.

881

882 **Author contributions**

883 PL and CS designed the experiments and PL carried them out. YS developed the modified  
884  $\delta$ HBV code. PL prepared the manuscript with contributions from all co-authors.

885

886 **Competing interests**

887 Chaopeng Shen and Kathryn Lawson have financial interests in HydroSapient, Inc., a  
888 company that could potentially benefit from the results of this research. This interest has been  
889 reviewed by the Pennsylvania State University in accordance with its individual conflict of  
890 interest policy for the purpose of maintaining the objectivity and the integrity of research. The  
891 other authors have no competing interests to declare.

892

893 **Acknowledgments**

894 PL, CS, and KL were supported by the Office of Biological and Environmental Research  
895 of the U.S. Department of Energy (contract no. DESC0016605). PJ and MP were also partially  
896 supported by California Department of Water Resources Atmospheric River Program Phase III  
897 (Grant 4600014294). YS and CS were partially supported by subaward A23-0252-S002 from  
898 the Cooperative Institute for Research to Operations in Hydrology (CIROH) through the  
899 National Oceanic and Atmospheric Administration (NOAA) Cooperative Agreement (Grant  
900 no. NA22NWS4320003).

901

## 902 **References**

903 Aboelyazeed, D., Xu, C., Hoffman, F. M., Liu, J., Jones, A. W., Rackauckas, C., Lawson, K.,  
904 and Shen, C.: A differentiable, physics-informed ecosystem modeling and learning framework  
905 for large-scale inverse problems: demonstration with photosynthesis simulations,  
906 Biogeosciences, 20, 2671–2692, <https://doi.org/10.5194/bg-20-2671-2023>, 2023.

907 Addor, N., Newman, A. J., Mizukami, N., and Clark, M. P.: The CAMELS data set: catchment  
908 attributes and meteorology for large-sample studies, Hydrol. Earth Syst. Sci., 21, 5293–5313,  
909 <https://doi.org/10.5194/hess-21-5293-2017>, 2017.

910 Aghakouchak, A. and Habib, E.: Application of a Conceptual Hydrologic Model in Teaching  
911 Hydrologic Processes, International Journal of Engineering Education, 26, 2010.

912 Bandai, T. and Ghezzehei, T. A.: Physics-informed neural networks with monotonicity  
913 constraints for Richardson-Richards equation: Estimation of constitutive relationships and soil  
914 water flux density from volumetric water content measurements, Water Resources Research,  
915 57, e2020WR027642, <https://doi.org/10.1029/2020wr027642>, 2021.

916 Beck, H. E., van Dijk, A. I. J. M., de Roo, A., Dutra, E., Fink, G., Orth, R., and Schellekens,  
917 J.: Global evaluation of runoff from 10 state-of-the-art hydrological models, Hydrology and  
918 Earth System Sciences, 21, 2881–2903, <https://doi.org/10.5194/hess-21-2881-2017>, 2017.

919 Beck, H. E., Pan, M., Lin, P., Seibert, J., Dijk, A. I. J. M. van, and Wood, E. F.: Global fully  
920 distributed parameter regionalization based on observed streamflow from 4,229 headwater  
921 catchments, Journal of Geophysical Research: Atmospheres, 125, e2019JD031485,  
922 <https://doi.org/10.1029/2019JD031485>, 2020.

923 Behnke, R., Vavrus, S., Allstadt, A., Albright, T., Thogmartin, W. E., and Radeloff, V. C.:  
924 Evaluation of downscaled, gridded climate data for the conterminous United States, Ecological  
925 Applications, 26, 1338–1351, <https://doi.org/10.1002/15-1061>, 2016.

926 Bell, V. A. and Moore, R. J.: The sensitivity of catchment runoff models to rainfall data at  
927 different spatial scales, Hydrology and Earth System Sciences, 4, 653–667,  
928 <https://doi.org/10.5194/hess-4-653-2000>, 2000.

929 [Bellmore, J. R., Duda, J. J., Craig, L. S., Greene, S. L., Torgersen, C. E., Collins, M. J., and](#)  
930 [Vittum, K.: Status and trends of dam removal research in the United States. Wiley](#)  
931 [Interdisciplinary Reviews: Water, 4, e1164, https://doi.org/10.1002/wat2.1164, 2017.](#)

932 Bergström, S.: Development and application of a conceptual runoff model for Scandinavian  
933 catchments, PhD Thesis, Swedish Meteorological and Hydrological Institute (SMHI),  
934 Norköping, Sweden, 1976.

935 Bergström, S.: The HBV model—its structure and applications, SMHI, 1992.

936 Bindas, T., Tsai, W.-P., Liu, J., Rahmani, F., Feng, D., Bian, Y., Lawson, K., and Shen, C.:  
937 Improving river routing using a differentiable Muskingum-Cunge model and physics-informed  
938 machine learning, *Water Resources Research*, 60, e2023WR035337,  
939 <https://doi.org/10.1029/2023WR035337>, 2024.

940 Bodnar, C., Bruinsma, W. P., Lucic, A., Stanley, M., Allen, A., Brandstetter, J., Garvan, P.,  
941 Riechert, M., Weyn, J. A., Dong, H., Gupta, J. K., Thambiratnam, K., Archibald, A. T., Wu,  
942 C.-C., Heider, E., Welling, M., Turner, R. E., and Perdikaris, P.: A foundation model for the  
943 Earth system, *Nature*, 641, 1180–1187, <https://doi.org/10.1038/s41586-025-09005-y>, 2025.

944 Brunner, M. I., Slater, L., Tallaksen, L. M., and Clark, M.: Challenges in modeling and  
945 predicting floods and droughts: A review, *WIREs Water*, 8, e1520,  
946 <https://doi.org/10.1002/wat2.1520>, 2021.

947 Clark, M. P., Slater, A. G., Rupp, D. E., Woods, R. A., Vrugt, J. A., Gupta, H. V., Wagener,  
948 T., and Hay, L. E.: Framework for Understanding Structural Errors (FUSE): A modular  
949 framework to diagnose differences between hydrological models, *Water Resources Research*,  
950 44, <https://doi.org/10/chvc6k>, 2008.

951 Clark, M. P., Nijssen, B., Lundquist, J. D., Kavetski, D., Rupp, D. E., Woods, R. A., Freer, J.  
952 E., Gutmann, E. D., Wood, A. W., Brekke, L. D., Arnold, J. R., Gochis, D. J., and Rasmussen,  
953 R. M.: A unified approach for process-based hydrologic modeling: 1. Modeling concept, *Water*  
954 *Resources Research*, 51, 2498–2514, <https://doi.org/10/f7db99>, 2015.

955 Clark, M. P., Wilby, R. L., Gutmann, E. D., Vano, J. A., Gangopadhyay, S., Wood, A. W.,  
956 Fowler, H. J., Prudhomme, C., Arnold, J. R., and Brekke, L. D.: Characterizing uncertainty of  
957 the hydrologic impacts of climate change, *Curr Clim Change Rep*, 2, 55–64,  
958 <https://doi.org/10.1007/s40641-016-0034-x>, 2016.

959 Dion, P., Martel, J.-L., and Arsenault, R.: Hydrological ensemble forecasting using a multi-  
960 model framework, *Journal of Hydrology*, 600, 126537,  
961 <https://doi.org/10.1016/j.jhydrol.2021.126537>, 2021.

962 Feng, D., Fang, K., and Shen, C.: Enhancing streamflow forecast and extracting insights using  
963 long-short term memory networks with data integration at continental scales, *Water Resources*  
964 *Research*, 56, e2019WR026793, <https://doi.org/10.1029/2019WR026793>, 2020.

965 Feng, D., Lawson, K., and Shen, C.: Mitigating prediction error of deep learning streamflow  
966 models in large data-sparse regions with ensemble modeling and soft data, *Geophysical*  
967 *Research Letters*, 48, e2021GL092999, <https://doi.org/10.1029/2021GL092999>, 2021.

968 Feng, D., Liu, J., Lawson, K., and Shen, C.: Differentiable, learnable, regionalized process-

969 based models with multiphysical outputs can approach state-of-the-art hydrologic prediction  
970 accuracy, *Water Resources Research*, 58, e2022WR032404,  
971 <https://doi.org/10.1029/2022WR032404>, 2022.

972 Feng, D., Shen, C., Liu, J., Lawson, K., and Beck, H.: differentiable parameter learning (dPL)  
973 + HBV hydrologic model, , <https://doi.org/10.5281/zenodo.7943626>, 2023a.

974 Feng, D., Beck, H., Lawson, K., and Shen, C.: The suitability of differentiable, physics-  
975 informed machine learning hydrologic models for ungauged regions and climate change impact  
976 assessment, *Hydrology and Earth System Sciences*, 27, 2357–2373,  
977 <https://doi.org/10.5194/hess-27-2357-2023>, 2023b.

978 Frame, J. M., Kratzert, F., Klotz, D., Gauch, M., Shalev, G., Gilon, O., Qualls, L. M., Gupta,  
979 H. V., and Nearing, G. S.: Deep learning rainfall-runoff predictions of extreme events,  
980 *Hydrology and Earth System Sciences*, 26, 3377–3392, <https://doi.org/10.5194/hess-26-3377-2022>, 2022.

982 Hanazaki, R., Yamazaki, D., and Yoshimura, K.: Development of a reservoir flood control  
983 scheme for global flood models, *JAMES*, 14, e2021MS002944,  
984 <https://doi.org/10.1029/2021MS002944>, 2022.

985 Hargreaves, G. H.: Defining and using reference evapotranspiration, *Journal of Irrigation and  
986 Drainage Engineering*, 120, 1132–1139, [https://doi.org/10.1061/\(ASCE\)0733-9437\(1994\)120:6\(1132\)](https://doi.org/10.1061/(ASCE)0733-9437(1994)120:6(1132)), 1994.

988 He, Y., Chen, M., Wen, Y., Duan, Q., Yue, S., Zhang, J., Li, W., Sun, R., Zhang, Z., Tao, R.,  
989 Tang, W., and Lü, G.: An open online simulation strategy for hydrological ensemble  
990 forecasting, *Environmental Modelling & Software*, 174, 105975,  
991 <https://doi.org/10.1016/j.envsoft.2024.105975>, 2024.

992 Heidari, H., Arabi, M., Warziniack, T., and Kao, S.-C.: Assessing shifts in regional  
993 hydroclimatic conditions of U.S. river basins in response to climate change over the 21st  
994 century, *Earth's Future*, 8, e2020EF001657, <https://doi.org/10.1029/2020EF001657>, 2020.

995 Hochreiter, S. and Schmidhuber, J.: Long Short-Term Memory, *Neural Computation*, 9, 1735–  
996 1780, <https://doi.org/10.1162/neco.1997.9.8.1735>, 1997.

997 Ji, H., Song, Y., Bindas, T., Shen, C., Yang, Y., Pan, M., Liu, J., Rahmani, F., Abbas, A., Beck,  
998 H., Lawson, K., and Wada, Y.: Distinct hydrologic response patterns and trends worldwide  
999 revealed by physics-embedded learning, *Nat. Commun.*, 16, 9169,  
1000 <https://doi.org/10.1038/s41467-025-64367-1>, 2025.

1001 Jiang, S., Zheng, Y., and Solomatine, D.: Improving AI system awareness of geoscience  
1002 knowledge: Symbiotic integration of physical approaches and deep learning, *Geophys. Res.  
1003 Lett.*, 47, e2020GL088229, <https://doi.org/10.1029/2020GL088229>, 2020.

1004 Kling, H., Fuchs, M., and Paulin, M.: Runoff conditions in the upper Danube basin under an  
1005 ensemble of climate change scenarios, *Journal of Hydrology*, 424–425, 264–277,  
1006 <https://doi.org/10.1016/j.jhydrol.2012.01.011>, 2012.

1007 Kraft, B., Jung, M., Körner, M., Koirala, S., and Reichstein, M.: Towards hybrid modeling of  
1008 the global hydrological cycle, *Hydrology and Earth System Sciences*, 26, 1579–1614,

1009 <https://doi.org/10.5194/hess-26-1579-2022>, 2022.

1010 Kratzert, F., Klotz, D., Brenner, C., Schulz, K., and Herrnegger, M.: Rainfall-Runoff modelling  
1011 using Long-Short-Term-Memory (LSTM) networks, *Hydrology and Earth System Sciences*,  
1012 22, 6005–6022, <https://doi.org/10.17605/OSF.IO/QV5JZ>, 2018.

1013 Kratzert, F., Klotz, D., Herrnegger, M., Sampson, A. K., Hochreiter, S., and Nearing, G. S.:  
1014 Toward improved predictions in ungauged basins: Exploiting the power of machine learning,  
1015 *Water Resources Research*, 55, 11344–11354, <https://doi.org/10/gg4ck8>, 2019.

1016 Kratzert, F., Klotz, D., Hochreiter, S., and Nearing, G. S.: A note on leveraging synergy in  
1017 multiple meteorological data sets with deep learning for rainfall–runoff modeling, *Hydrology*  
1018 and *Earth System Sciences*, 25, 2685–2703, <https://doi.org/10.5194/hess-25-2685-2021>, 2021.

1019 Kratzert, F., Gauch, M., Nearing, G., and Klotz, D.: NeuralHydrology — A Python library for  
1020 Deep Learning research in hydrology, <https://doi.org/10.5281/zenodo.6326394>, 2022.

1021 Leube, P. C., de Barros, F. P. J., Nowak, W., and Rajagopal, R.: Towards optimal allocation of  
1022 computer resources: Trade-offs between uncertainty quantification, discretization and model  
1023 reduction, *Environmental Modelling & Software*, 50, 97–107,  
1024 <https://doi.org/10.1016/j.envsoft.2013.08.008>, 2013.

1025 Li, P., Zha, Y., Shi, L., Tso, C. H. M., Zhang, Y., and Zeng, W.: Comparison of the use of a  
1026 physical-based model with data assimilation and machine learning methods for simulating soil  
1027 water dynamics, *Journal of Hydrology*, 584, 124692,  
1028 <https://doi.org/10.1016/j.jhydrol.2020.124692>, 2020a.

1029 Li, P., Zha, Y., Tso, C. H. M., Shi, L., Yu, D., Zhang, Y., and Zeng, W.: Data assimilation of  
1030 uncalibrated soil moisture measurements from frequency-domain reflectometry, *Geoderma*,  
1031 374, 114432, <https://doi.org/10.1016/j.geoderma.2020.114432>, 2020b.

1032 Li, P., Zha, Y., Shi, L., and Zhong, H.: Identification of the terrestrial water storage change  
1033 features in the North China Plain via independent component analysis, *Journal of Hydrology: Regional Studies*, 38, 100955, <https://doi.org/10.1016/j.ejrh.2021.100955>, 2021.

1035 Li, P., Zha, Y., Shi, L., and Zhong, H.: Assessing the Global Relationships Between  
1036 Teleconnection Factors and Terrestrial Water Storage Components, Water Resources  
1037 Management, 36, 119–133, <https://doi.org/10.1007/s11269-021-03015-x>, 2022.

1038 Li, P., Zha, Y., Zuo, B., and Zhang, Y.: A family of soil water retention models based on  
1039 sigmoid functions, *Water Resources Research*, 59, e2022WR033160,  
1040 <https://doi.org/10.1029/2022WR033160>, 2023a.

1041 Li, P., Zha, Y., and Tso, C.-H. M.: Reconstructing GRACE-derived terrestrial water storage  
1042 anomalies with in-situ groundwater level measurements and meteorological forcing data,  
1043 *Journal of Hydrology: Regional Studies*, 50, 101528,  
1044 <https://doi.org/10.1016/j.ejrh.2023.101528>, 2023b.

1045 Li, P., Zha, Y., Zhang, Y., Michael Tso, C.-H., Attinger, S., Samaniego, L., and Peng, J.: Deep  
1046 learning integrating scale conversion and pedo-transfer function to avoid potential errors in  
1047 cross-scale transfer, *Water Resources Research*, 60, e2023WR035543,  
1048 <https://doi.org/10.1029/2023WR035543>, 2024.

1049 Lin, Y., Wang, D., Zhu, J., Sun, W., Shen, C., and Shangguan, W.: Development of objective  
1050 function-based ensemble model for streamflow forecasts, *Journal of Hydrology*, 632, 130861,  
1051 <https://doi.org/10.1016/j.jhydrol.2024.130861>, 2024.

1052 Lins, H. F. and Slack, J. R.: Streamflow trends in the United States, *Geophysical Research  
1053 Letters*, 26, 227–230, <https://doi.org/10.d5zbbd>, 1999.

1054 Liu, J., Rahmani, F., Lawson, K., and Shen, C.: A multiscale deep learning model for soil  
1055 moisture integrating satellite and in situ data, *Geophysical Research Letters*, 49,  
1056 e2021GL096847, <https://doi.org/10.1029/2021GL096847>, 2022.

1057 Liu, J., Bian, Y., Lawson, K., and Shen, C.: Probing the limit of hydrologic predictability with  
1058 the Transformer network, *Journal of Hydrology*, 637, 131389,  
1059 <https://doi.org/10.1016/j.jhydrol.2024.131389>, 2024.

1060 Mai, J., Craig, J. R., Tolson, B. A., and Arsenault, R.: The sensitivity of simulated streamflow  
1061 to individual hydrologic processes across North America, *Nat Commun*, 13, 455,  
1062 <https://doi.org/10.1038/s41467-022-28010-7>, 2022.

1063 Maurer, E. P., Wood, A. W., Adam, J. C., Lettenmaier, D. P., and Nijssen, B.: A long-term  
1064 hydrologically based dataset of land surface fluxes and states for the conterminous United  
1065 States, *Journal of Climate*, 15, 3237–3251, [https://doi.org/10.1175/1520-0442\(2002\)015<3237:ALTHBD>2.0.CO;2](https://doi.org/10.1175/1520-0442(2002)015<3237:ALTHBD>2.0.CO;2), 2002.

1067 Moges, E., Demissie, Y., and Li, H.-Y.: Hierarchical mixture of experts and diagnostic  
1068 modeling approach to reduce hydrologic model structural uncertainty, *Water Resources  
1069 Research*, 52, 2551–2570, <https://doi.org/10.1002/2015WR018266>, 2016.

1070 Nai, C., Liu, X., Tang, Q., Liu, L., Sun, S., and Gaffney, P. P. J.: A novel strategy for automatic  
1071 selection of cross-basin data to improve local machine learning-based runoff models, *Water  
1072 Resources Research*, 60, e2023WR035051, <https://doi.org/10.1029/2023WR035051>, 2024.

1073 Narkhede, M. V., Bartakke, P. P., and Sutaone, M. S.: A review on weight initialization  
1074 strategies for neural networks, *Artificial Intelligence Review*, 55, 291–322,  
1075 <https://doi.org/10.1007/s10462-021-10033-z>, 2022.

1076 Nash, J. E. and Sutcliffe, J. V.: River flow forecasting through conceptual models part I — A  
1077 discussion of principles, *Journal of Hydrology*, 10, 282–290, [https://doi.org/10.1016/0022-1694\(70\)90255-6](https://doi.org/10.1016/0022-<br/>1078 1694(70)90255-6), 1970.

1079 Nearing, G., Cohen, D., Dube, V., Gauch, M., Gilon, O., Harrigan, S., Hassidim, A., Klotz, D.,  
1080 Kratzert, F., Metzger, A., Nevo, S., Pappenberger, F., Prudhomme, C., Shalev, G., Shenzis, S.,  
1081 Tekalign, T. Y., Weitzner, D., and Matias, Y.: Global prediction of extreme floods in ungauged  
1082 watersheds, *Nature*, 627, 559–563, <https://doi.org/10.1038/s41586-024-07145-1>, 2024.

1083 Newman, A. J. and Clark, M.: A large-sample watershed-scale hydrometeorological dataset for  
1084 the contiguous USA, <https://doi.org/10.5065/D6MW2F4D>, 2014.

1085 Newman, A. J., Mizukami, N., Clark, M. P., Wood, A. W., Nijssen, B., Nearing, G., Newman,  
1086 A. J., Mizukami, N., Clark, M. P., Wood, A. W., Nijssen, B., and Nearing, G.: Benchmarking  
1087 of a Physically Based Hydrologic Model, *Journal of Hydrometeorology*, 18, 2215–2225,  
1088 <https://doi.org/10.gbw9s>, 2017.

1089 Newman, A. J., Clark, M. P., Longman, R. J., and Giambelluca, T. W.: Methodological  
1090 intercomparisons of station-based gridded meteorological products: Utility, limitations, and  
1091 paths forward, <https://doi.org/10.1175/JHM-D-18-0114.1>, 2019.

1092 Ouyang, W., Lawson, K., Feng, D., Ye, L., Zhang, C., and Shen, C.: Continental-scale  
1093 streamflow modeling of basins with reservoirs: Towards a coherent deep-learning-based  
1094 strategy, *Journal of Hydrology*, 599, 126455, <https://doi.org/10.1016/j.jhydrol.2021.126455>,  
1095 2021.

1096 Paul, P. K., Zhang, Y., Ma, N., Mishra, A., Panigrahy, N., and Singh, R.: Selecting hydrological  
1097 models for developing countries: Perspective of global, continental, and country scale models  
1098 over catchment scale models, *Journal of Hydrology*, 600, 126561,  
1099 <https://doi.org/10.1016/j.jhydrol.2021.126561>, 2021.

1100 Rahmani, F., Appling, A., Feng, D., Lawson, K., and Shen, C.: Identifying structural priors in  
1101 a hybrid differentiable model for stream water temperature modeling, *Water Resources  
1102 Research*, 59, e2023WR034420, <https://doi.org/10.1029/2023WR034420>, 2023.

1103 Reichle, R. H. and Koster, R. D.: Assessing the impact of horizontal error correlations in  
1104 background fields on soil moisture estimation, *Journal of Hydrometeorology*, 4, 1229–1242,  
1105 [https://doi.org/10.1175/1525-7541\(2003\)004<1229:ATIOHE>2.0.CO;2](https://doi.org/10.1175/1525-7541(2003)004<1229:ATIOHE>2.0.CO;2), 2003.

1106 ~~Ryan Bellmore, J., Duda, J. J., Craig, L. S., Greene, S. L., Torgersen, C. E., Collins, M. J., and  
1107 Vittum, K.: Status and trends of dam removal research in the United States, *WIREs Water*, 4,  
1108 e1164, <https://doi.org/10.1002/wat2.1164>, 2017.~~

1109 Sawadekar, K., Song, Y., Pan, M., Beck, H., McCrary, R., Ullrich, P., Lawson, K., and Shen,  
1110 C.: Improving differentiable hydrologic modeling with interpretable forcing fusion, *J. Hydrol.*,  
1111 659, 133320, <https://doi.org/10.1016/j.jhydrol.2025.133320>, 2025.

1112 Shen, C., Appling, A. P., Gentine, P., Bandai, T., Gupta, H., Tartakovsky, A., Baity-Jesi, M.,  
1113 Fenicia, F., Kifer, D., Li, L., Liu, X., Ren, W., Zheng, Y., Harman, C. J., Clark, M., Farthing,  
1114 M., Feng, D., Kumar, P., Aboelyazeed, D., Rahmani, F., Song, Y., Beck, H. E., Bindas, T.,  
1115 Dwivedi, D., Fang, K., Höge, M., Rackauckas, C., Mohanty, B., Roy, T., Xu, C., and Lawson,  
1116 K.: Differentiable modelling to unify machine learning and physical models for geosciences,  
1117 *Nat Rev Earth Environ*, 4, 552–567, <https://doi.org/10.1038/s43017-023-00450-9>, 2023.

1118 Solanki, H., Vegad, U., Kushwaha, A., and Mishra, V.: Improving streamflow prediction using  
1119 multiple hydrological models and machine learning methods, *Water Resources Research*, 61,  
1120 e2024WR038192, <https://doi.org/10.1029/2024WR038192>, 2025.

1121 Song, Y., Bindas, T., Shen, C., Ji, H., Knoben, W. J. M., Lonzarich, L., Clark, M. P., Liu, J.,  
1122 van Werkhoven, K., Lemont, S., Denno, M., Pan, M., Yang, Y., Rapp, J., Kumar, M., Rahmani,  
1123 F., Thébault, C., Sawadekar, K., and Lawson, K.: High-resolution national-scale water  
1124 modeling is enhanced by multiscale differentiable physics-informed machine learning,  
1125 <https://doi.org/10.22541/essoar.172736277.74497104/v1>, 26 September 2024a.

1126 Song, Y., Knoben, W. J. M., Clark, M. P., Feng, D., Lawson, K., Sawadekar, K., and Shen, C.:  
1127 When ancient numerical demons meet physics-informed machine learning: adjoint-based  
1128 gradients for implicit differentiable modeling, *Hydrology and Earth System Sciences*, 28,  
1129 3051–3077, <https://doi.org/10.5194/hess-28-3051-2024>, 2024b.

1130 Song, Y., Bindas, T., Shen, C., Ji, H., Knoben, W. J. M., Lonzarich, L., Clark, M. P., Liu, J.,  
1131 van Werkhoven, K., Lamont, S., Denno, M., Pan, M., Yang, Y., Rapp, J., Kumar, M., Rahmani,  
1132 F., Thébault, C., Adkins, R., Halgren, J., Patel, T., Patel, A., Sawadekar, K. A., and Lawson,  
1133 K.: High-resolution national-scale water modeling is enhanced by multiscale differentiable  
1134 physics-informed machine learning, *Water Resour. Res.*, 61, e2024WR038928,  
1135 <https://doi.org/10.1029/2024WR038928>, 2025a.

1136 Song, Y., Sawadekar, K., Frame, J. M., Pan, M., Clark, M., Knoben, W. J. M., Wood, A. W.,  
1137 Lawson, K. E., Patel, T., and Shen, C.: Physics-informed, differentiable hydrologic models for  
1138 capturing unseen extreme events, <https://doi.org/10.22541/essoar.172304428.82707157/v2>,  
1139 2025b.

1140 Thornton, P. E., Running, S. W., and White, M. A.: Generating surfaces of daily meteorological  
1141 variables over large regions of complex terrain, *Journal of Hydrology*, 190, 214–251,  
1142 [https://doi.org/10.1016/S0022-1694\(96\)03128-9](https://doi.org/10.1016/S0022-1694(96)03128-9), 1997.

1143 Tsai, W.-P., Feng, D., Pan, M., Beck, H., Lawson, K., Yang, Y., Liu, J., and Shen, C.: From  
1144 calibration to parameter learning: Harnessing the scaling effects of big data in geoscientific  
1145 modeling, *Nat Commun*, 12, 5988, <https://doi.org/10.1038/s41467-021-26107-z>, 2021.

1146 Wada, Y., de Graaf, I. E. M., and van Beek, L. P. H.: High-resolution modeling of human and  
1147 climate impacts on global water resources, *Journal of Advances in Modeling Earth Systems*, 8,  
1148 735–763, <https://doi.org/10.1029/2016MS001080>, 2016.

1149 Wang, N., Zhang, D., Chang, H., and Li, H.: Deep learning of subsurface flow via theory-  
1150 guided neural network, *Journal of Hydrology*, 584, 124700,  
1151 <https://doi.org/10.1016/j.jhydrol.2020.124700>, 2020.

1152 West, B. D., Maxwell, R. M., and Condon, L. E.: A scalable and modular reservoir  
1153 implementation for large-scale integrated hydrologic simulations, *Hydrology and Earth System  
1154 Sciences*, 29, 245–259, <https://doi.org/10.5194/hess-29-245-2025>, 2025.

1155 Wilbrand, K., Taormina, R., ten Veldhuis, M.-C., Visser, M., Hrachowitz, M., Nuttall, J., and  
1156 Dahm, R.: Predicting streamflow with LSTM networks using global datasets, *Front. Water*, 5,  
1157 <https://doi.org/10.3389/frwa.2023.1166124>, 2023.

1158 Xia, Y., Mitchell, K., Ek, M., Sheffield, J., Cosgrove, B., Wood, E., Luo, L., Alonge, C., Wei,  
1159 H., Meng, J., Livneh, B., Lettenmaier, D., Koren, V., Duan, Q., Mo, K., Fan, Y., and Mocko,  
1160 D.: Continental-scale water and energy flux analysis and validation for the North American  
1161 Land Data Assimilation System project phase 2 (NLDAS-2): 1. Intercomparison and  
1162 application of model products, *Journal of Geophysical Research: Atmospheres*, 117,  
1163 <https://doi.org/10.1029/2011JD016048>, 2012.

1164 Xie, K., Liu, P., Zhang, J., Han, D., Wang, G., and Shen, C.: Physics-guided deep learning for  
1165 rainfall-runoff modeling by considering extreme events and monotonic relationships, *Journal  
1166 of Hydrology*, 603, 127043, <https://doi.org/10.1016/j.jhydrol.2021.127043>, 2021.

1167 Yao, L., Libera, D. A., Kheimi, M., Sankarasubramanian, A., and Wang, D.: The roles of  
1168 climate forcing and its variability on streamflow at daily, monthly, annual, and long-term scales,  
1169 *Water Resources Research*, 56, e2020WR027111, <https://doi.org/10.1029/2020WR027111>,  
1170 2020.

1171 Yilmaz, K. K., Gupta, H. V., and Wagener, T.: A process-based diagnostic approach to model  
1172 evaluation: Application to the NWS distributed hydrologic model, *Water Resources Research*,  
1173 44, <https://doi.org/10/fpvsgb>, 2008.

1174 Yu, D., Yang, J., Shi, L., Zhang, Q., Huang, K., Fang, Y., and Zha, Y.: On the uncertainty of  
1175 initial condition and initialization approaches in variably saturated flow modeling, *Hydrology*  
1176 and *Earth System Sciences*, 23, 2897–2914, <https://doi.org/10.5194/hess-23-2897-2019>, 2019.

1177 Yu, M., Huang, Q., and Li, Z.: Deep learning for spatiotemporal forecasting in Earth system  
1178 science: a review, *International Journal of Digital Earth*, 17, 2391952,  
1179 <https://doi.org/10.1080/17538947.2024.2391952>, 2024.

1180 Zhang, Q., Shi, L., Holzman, M., Ye, M., Wang, Y., Carmona, F., and Zha, Y.: A dynamic  
1181 data-driven method for dealing with model structural error in soil moisture data assimilation,  
1182 *Advances in Water Resources*, 132, 103407, <https://doi.org/10.1016/j.advwatres.2019.103407>,  
1183 2019.

1184 Zounemat-Kermani, M., Batelaan, O., Fadaee, M., and Hinkelmann, R.: Ensemble machine  
1185 learning paradigms in hydrology: A review, *Journal of Hydrology*, 598, 126266,  
1186 <https://doi.org/10.1016/j.jhydrol.2021.126266>, 2021.

1187

1188